Alexandria Engineering Journal (2023) 68, 343–364

HOSTED BY

Alexandria University

Alexandria Engineering Journal

www.elsevier.com/locate/aej
www.sciencedirect.com

ORIGINAL ARTICLE

Aerodynamic impacts of high-speed trains on city-oriented noise barriers: A moving model experiment

Yikang Liu [a], Weichao Yang [a,b], E Deng [c,d,*], Youwu Wang [c,d], Xuhui He [a,b], Yongming Huang [a], Zhengwei Chen [c,d]

[a] School of Civil Engineering, Central South University, Changsha, PR China
[b] National Engineering Research Center of High-speed Railway Construction Technology, Changsha, PR China
[c] National Rail Transit Electrification and Automation Engineering Technology Research Center (Hong Kong Branch), Hong Kong, PR China
[d] Department of Civil and Environmental Engineering, The Hong Kong Polytechnic University, Hong Kong, PR China

Received 22 October 2022; revised 6 January 2023; accepted 18 January 2023
Available online 24 January 2023

KEYWORDS

City-oriented noise barriers;
High-speed trains;
Moving model experiment;
Aerodynamic impacts;
Dominant frequency

Abstract Two types of city-oriented noise barriers, i.e., fully-enclosed noise barrier and bilateral inverted L-shaped semi-enclosed noise barrier, have been gradually adopted in city centres along high-speed railways to reduce noise pollution. The aerodynamic impacts of high-speed trains present a threat to the long-term durability of the city-oriented noise barriers. To promote the usage and increase the sustainability of city-oriented noise barriers, a moving-model experiment system with city-oriented noise barriers and HST with a scale ratio of 1:16.8 is established. The train type is CRH380A and the train speed is up to 350 km/h. A systematic comparative study on the aerodynamic performance of the two types of city-oriented noise barriers is conducted. The similarities and differences of transient pressure time–histories, spatial distribution of pressure peaks and spectral characteristics of aerodynamic pressure acting on the two types of noise barriers are compared and discussed. Moreover, the influence of train speed on the characteristics of the train-induced aerodynamic pressure is also investigated. The results show that the pressure fluctuation of the two types of noise barriers is caused by different reasons. Compared with the fully-enclosed noise barrier, the transient pressure of the semi-enclosed noise barrier is more sensitive to train speeds. The research results may provide a reference for the engineering design of city-oriented noise barriers on high-speed railways.

1. Introduction

Noise barriers have been widely applied to reduce noise pollution caused by the high-speed train (HST), driven by the densification of railway network and the improving requirement

* Corresponding author at: National Rail Transit Electrification and Automation Engineering Technology Research Center (Hong Kong Branch), Hong Kong, PR China.
E-mail address: early.deng@polyu.edu.hk (E Deng).
Peer review under responsibility of Faculty of Engineering, Alexandria University.

https://doi.org/10.1016/j.aej.2023.01.041
1110-0168

for high-standard life [1–4]. As reported by Li et al., the high-speed operating train induces an unacceptable noise to the environment [5,6]. Vertical noise barriers are a traditional type of noise barriers and normally installed near noise-sensitive places, such as schools, factories and dispersed residential areas. The vertical noise barrier receives most frequent application on high-speed railway because of the low height (generally 2.15–3.15 m), simple structure and convenience of installation [7–9]. However, the traditional vertical noise barrier shows limited noise reduction capacity, especially in high sensitivity areas of noise. When tall buildings are built along the railway, the traditional vertical noise barrier has almost no noise reduction effect on high floors. Given this situation, two types of city-oriented noise barriers, i.e., fully-enclosed noise barrier with rectangular cross-section (FENBRC) and bilateral inverted L-shaped semi-enclosed noise barrier (BILSENB) have been gradually adopted along the high-speed railway to meet the increasing demand for noise reduction, as shown in Fig. 1 [10]. Compared with the vertical noise barrier, the two types of city-oriented noise barriers show better noise reduction performance due to their sealing capacity, which is more suitable for regions with high requirements for noise reduction, especially in city centres and densely populated areas [11,12].

When the HST passes the noise barrier at high speeds, the strong disturbance of air flow caused by the train movement will produce transient pressure impacts on the noise barrier [3,12–14]. Long-term cyclic impacts of the transient pressure may cause unreasonable vibration damages or even serious fatigue failures. In 2003, the noise barrier installed on the railway between Cologne and Frankfurt in Germany broke under the action of transient pressure load generated by HST, resulting in serious deformation of aluminium alloy plate and loosening of connection ribs between steel column and fixed support [7,15]. Passing HSTs presents more serious aerodynamic impacts on the FENBRC and BILSENB because they have a narrower internal space and a significantly larger area of loading surface compared with traditional vertical noise barriers. In addition, intense resonance effects may occur when the dominant frequency of train-induced fluctuating pressure is close to or equal to the natural vibration frequency of the noise barrier, further aggravating the damage of the noise barrier and reducing the service life. Due to the increasing speed of HSTs in China, the aerodynamic impact generated by HSTs on the two types of noise barriers becomes a major controlling factor in the structural design and material selection.

In view of the aerodynamic impact of trains passing by trackside structures, including steel frames, partially-enclosed spaces, overpass bridges, screen doors, etc., extensive studies were carried out by field measurement, indoor model experiment and numerical simulation [16–21]. Carassale and Brunenghi experimented the structural displacement caused by the aerodynamic and seismic effects of a 7 m-high frame when the train speed is 150 km/h [22]. A dimensionless model is proposed for calculating the aerodynamic response of the trackside structure. The results showed that the peak displacement at the top of the steel frame caused by the aerodynamic impact is 2–3 times that of the train-induced seismic. Gilbert et al. conducted a 1:25 moving-model experiment to investigate the aerodynamic loads of passing trains exerted on partially-enclosed spaces, double vertical walls and tunnels [23]. Baker et al. performed a 1:25 model experiment to investigate the aerodynamic loads of trestle platforms, station canopies, overbridges and vertical hoardings when trains with three head types passed by [24]. The measured aerodynamic pressure has two positive and two negative peaks, which changing with the infrastructure type, the location of measurement point and the type of train head. Yang et al. studied the aerodynamic load characteristics of trains passing through a cross-street overpass at a speed of 250–350 km/h through CFD simulations [16]. The results showed that the peak pressure linearly decreases vertically. The maximum pressure attenuation rate in the horizontal direction is large in the range of 15 m from the track center line and gradually decreases with the increase in the horizontal distance. Rocchi et al. carried out a series of field experiments on an Italian railway line and studied the influence of three train types on aerodynamic loads of the trackbed, slipstream effects and time–histories of the head pulse [25]. The results showed that different degrees of aerodynamic impacts were caused by the train on different infrastructures. Liang et al. conducted a dynamic model research on aerodynamic load variation characteristics of an overpass when HSTs pass through [26]. They pointed out that the outer open air slightly affects the attenuation law of train-induced pressure at the exit and entrance at the bottom region, resulting in a peak pressure lower than that of the central bottom region. Zeng et al. conducted a 1/20 moving-model experiment on the aerodynamic pressure characteristic of subway screen doors caused by the metro train [27]. Two positive peak pressures were found to act on the screen door. The first peak was caused by the compressive wave when the train runs in the tun-

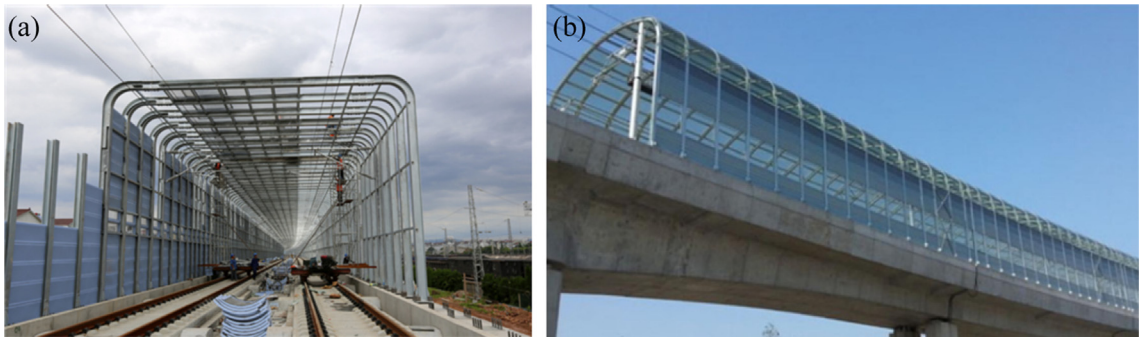

Fig. 1 Two types of city-oriented noise barriers: (a) FENBRC; (b) BILSENB [10].

nel, and the second peak was due to the passing of the train head.

Researchers also studied the fluctuating pressure characteristic caused by HSTs on traditional vertical noise barriers along the railway line. Xiong et al. performed a series of field measurements to investigate the transient pressure on a vertical barrier on a bridge [7,19]. Two HSTs with different streamlined head carriages with speed ranging from 250 km/h to 420 km/h were involved in the field experiment. They found that the peak-to-peak pressure on the inner surface of the noise barrier increases with the decrease in height, whereas the value on the outer surface decreases. The spectral analysis indicated that the primary frequency of HST-induced aerodynamic is approximately 4 Hz. Lv et al. experimented the strain response of a 2.15 m-high a 3.95 m-high barrier when two types of EMU pass at a speed of 270–395 km/h [28]. The strength of aerodynamic load on the entire surface increased with the train speed. Moreover, the positive strain amplitude is two times of the negative strain amplitude. Considering the high cost and low repeatability of field measurements, an indoor moving model experiment is an excellent research tool. Du et al. compared the pressure variation of two noise barriers with different heights based on a 1/20 moving-model experiment [29]. The pressure amplitude increased by 10.6 % and 14.1 % when the noise barrier height increases from 0.125 m to 0.25 m. Based on the research results in [29], we may intuitively speculate that the train-induced aerodynamic impact on the noise barrier intensifies with the restriction of noise barriers on the space around the train. Accordingly, the variation of flow field inside the FENBRC may be similar to that inside the high-speed. Zhang et al. investigated the effect of different portal types on the transient pressure and micropressure wave when the train enters the tunnel through a 1:20 moving model experiment [30]. Another similar moving model experiment performed by Zhang et al. focused on the transient pressure caused by trains on the tunnel surface [31]. They found that the difference in pressure amplitude values between the measuring points was mainly dependent on the negative pressure peak of the measuring points. Wang et al. investigated the effect of non-circular linings on the transient pressure inside the tunnel using a moving model experiment [32]. The longitudinal and circumferential distribution of the non-circular linings was found to have a significant influence on the characteristics of the pressure amplitude and initial compression wave induced by a train. Table 1 summarises the research method, object of research, train type, train speed and key findings of the above literature. Three main findings can be obtained from the references listed in Table 1: (1) The characteristic of train-induced aerodynamic pressure varies with the infrastructure type; (2) The aerodynamic impact increases with the increase in the train speed; (3) The aerodynamic impact of HSTs should not be ignored when designing the trackside structures.

To sum up, the main research gap of the literature includes two aspects: (1) The aerodynamic influences of HSTs on the FENBRC and BILSENB has not been reported previously; (2) The spatial and spectral characteristics as well as the train speed effect of the HST-induced pressure on the FENBRC and BILSENB have not been studied thoroughly. Noticing the engineering applications of city-oriented noise barriers in railways, a systematic comparison of the aerodynamic performance between them is a necessary to ensure their stability and safety.

A moving-model experiment system with city-oriented noise barriers and HST is established to investigate the difference in the aerodynamic performance of two types of city-oriented noise barriers when the HST passes by. The scale ratio is 1:16.8 and the train speed is up to 350 km/h. The similarities and differences of transient pressure time–histories, spatial distribution of pressure peaks and spectral characteristics of aerodynamic pressure acting on the two types of noise barriers are compared and discussed. Moreover, the influence of train speed on the characteristics of the train-induced aerodynamic pressure is also investigated.

2. Experiment method

2.1. Power system of the moving-model rig

The moving-model experiment is conducted in the Key Laboratory of Track Traffic Safety in Central South University. The moving-model rig is 164 m long and can launch the train to 500 km/h [30]. Fig. 2 shows the power system of the moving-model rig. The moving-model rig is divided into upper and lower layers. As shown in Fig. 2(a), the experimental layer is consisted by three sections, i.e., the acceleration section, test section and braking section. Before the experiment, the HST model is placed on the track of the acceleration section. The scaled noise barrier model is set on the test section. During the experiment, the rubber rope will be stretched to provide energy to the HST model. When the HST arrives at the test section, the hook releases and the HST run with inertia. More detailed setups of this moving-model system were reported in [30].

2.2. HST and noise barrier model

As shown in Fig. 3, the HST model used in this study is organised by three carriages and designed with a scale ratio of 1:16.8 based on the CRH380A, which is widely used in China's high-speed railways. We decided to test three carriages instead of eight or 16 for two reasons: (1) To reduce the weight of the HST. The rubber rope is the key component to provide kinetic energy for the HST model in the experiment. Hundreds of repeated tests must be conducted to obtain ideal results, indicating that the rubber was stretched for hundreds of times. A heavy HST model will reduce the life of the rubber rope. (2) To achieve a stable speed. The HST model runs with inertia after the rubber provides an initial speed. In this case, the heavier the HST model, the larger the friction is, resulting in a faster decrease in the speed. Then, the distortion of results may be induced. The characteristic height and width of the HST is H and $0.91H$ (H = 0.22 m). The lengths of the head, middle and tail carriage are L (L = 1.58 m), $0.94L$ and L, respectively, and the total length of the HST is $2.94L$. The HST model is fabricated by 3D printing to achieve a high smoothness and streamlined train surface. The lightweight high strength foam is chosen as the main material of the train body, and the weight of the HST model is 25 kg. The maximum design speed of all operating railways in China is 350 km/h. The HSTs in China are normally operating at a speed of 250 km/h to 350 km/h.

Table 1 Studies regarding the aerodynamic impact of passing trains on trackside structures.

Study	Author and year	Method	Types of trackside structure	Train type	Maximum train speed (km/h)	Key findings
1	Carassale and Brunenghi (2013) [22]	Field measurement	Steel frame	ETR 450	170	The aerodynamic response is 2–3 times of the train seismic response.
2	Gilbert et al. (2013) [23]	Moving model experiment	Partially-enclosed space, double vertical wall and tunnel	German ICE2	115	Different structure suffers different aerodynamic loads.
3	Baker et al. (2014) [24]	Moving model experiment	Trestle platform, station canopy, overpass bridge and vertical hoarding	Class 390, Class 158 and Class 66	144	The aerodynamic pressure changes with infrastructure types, measurement locations and train types.
4	Yang et al. (2015) [16]	Numerical simulation	Overpass bridge	CRH380	350	The maximum pressure decreases with the increase in the horizontal distance.
5	Liang et al. (2020) [26]	Moving model experiment	Overpass bridge	Chinese EMU	300	The peak pressure at the exit and entrance is lower than that of the central region
6	Zeng et al. (2021) [27]	Moving model experiment	Subway screen door	Type A + subway train	140	Two positive peak pressures act on the screen door.
7	Rocchi et al. (2018) [25]	Field measurement	Trackbed and vertical noise barrier	Confidential	300	Different structure suffers different aerodynamic loads.
8	Xiong et al. (2018, 2020) [7,19]	Field measurement	Vertical noise barrier	CRH380A and CRH380B	420	The primary frequency of HST-induced aerodynamic is approximately 4 Hz.
9	Lü et al. (2018) [28]	Field measurement	Vertical noise barrier	CRH380A and CRH380AM	320	The strength of aerodynamic load increases with the train speed.
10	Du et al. (2020) [29]	Moving model experiment	Vertical noise barrier	CRH	350	The pressure amplitude increases by 10.6 % and 14.1 % when the noise barrier height increases from 0.125 m to 0.25 m.
11	Zhang et al. (2017) [30]	Moving model experiment	Tunnel	CRH	350	The portal types have an influence on the transient pressure and micropressure wave.
12	Zhang et al. (2019) [20]	Moving model experiment	Tunnel	CRH	350	The difference in pressure amplitude values is mainly dependent on the negative pressure peak.
13	Wang et al. (2021) [32]	Numerical simulation	Tunnel	Not mentioned	350	The non-circular linings have a significant influence on the pressure amplitude and initial compression wave.

Therefore, the train speed is 250–350 km/h during the experiment.

The scale ratio of the noise barrier model is also 1:16.8, as shown in Fig. 4. The full length of the noise barrier model is 14.78L, and the height and width of the inner sketch are 2.2H and 3.2H, respectively. Twenty-six ribs are fixed equidistant longitudinally of all barrier models to ensure the stability of the noise barrier structure. The opening depth at the entrance and exit of the FENBRC is 0 or 1.84L, and the opening width ranges from 0 to 1.5H. The opening width at the top of the BILSENB is 2.0H. The top opening width size is used to distinguish noise barrier types. We use D and d followed after FENBRC and BILSENB, respectively. D greater than 0 means the FENBRC is opened in the roof at the entrance and exit, and d greater than 0 means the noise barrier is BILSENB. For example, FENBRC$_{(D=0.5H,\ d=0)}$ means the FENBRC has a top opening with a width of 0.5H at the entrance and exit; BILSENB $_{(D=0,\ d=2.0H)}$ means the BILSENB has a top opening with a width of 2.0H in the roof. Especially, FENBRC$_{(D=0,\ d=0)}$ means there is no gap in the roof of the FENBRC. In engineering practices, the FENBRC may be designed with roof openings at the entrance and exit to reduce the micro-pressure wave. Hence, we decided to test three more cases of the FENBRC. A total of nine cases are designed, including six FENBRC cases (three cases with roof openings at the entrance and exit) and three BILSENB cases. The detailed information of each case is shown in Table 2.

2.3. Discussion on experiment similarity criterion

The Reynolds number Re is a key index characterising the effect of fluid viscosity, as expressed by Eq. (1). The influence of Reynolds number on the flow field should be kept in a controllable range [33,34].

$$\mathrm{Re} = \rho V S/\mu \tag{1}$$

where ρ is the air density and ρ = 1.225 kg/m^3; V is the speed of the HST in m/s and the lowest speed of 250 km/h (V = 69.44 m/s) is considered here; S is the characteristic size

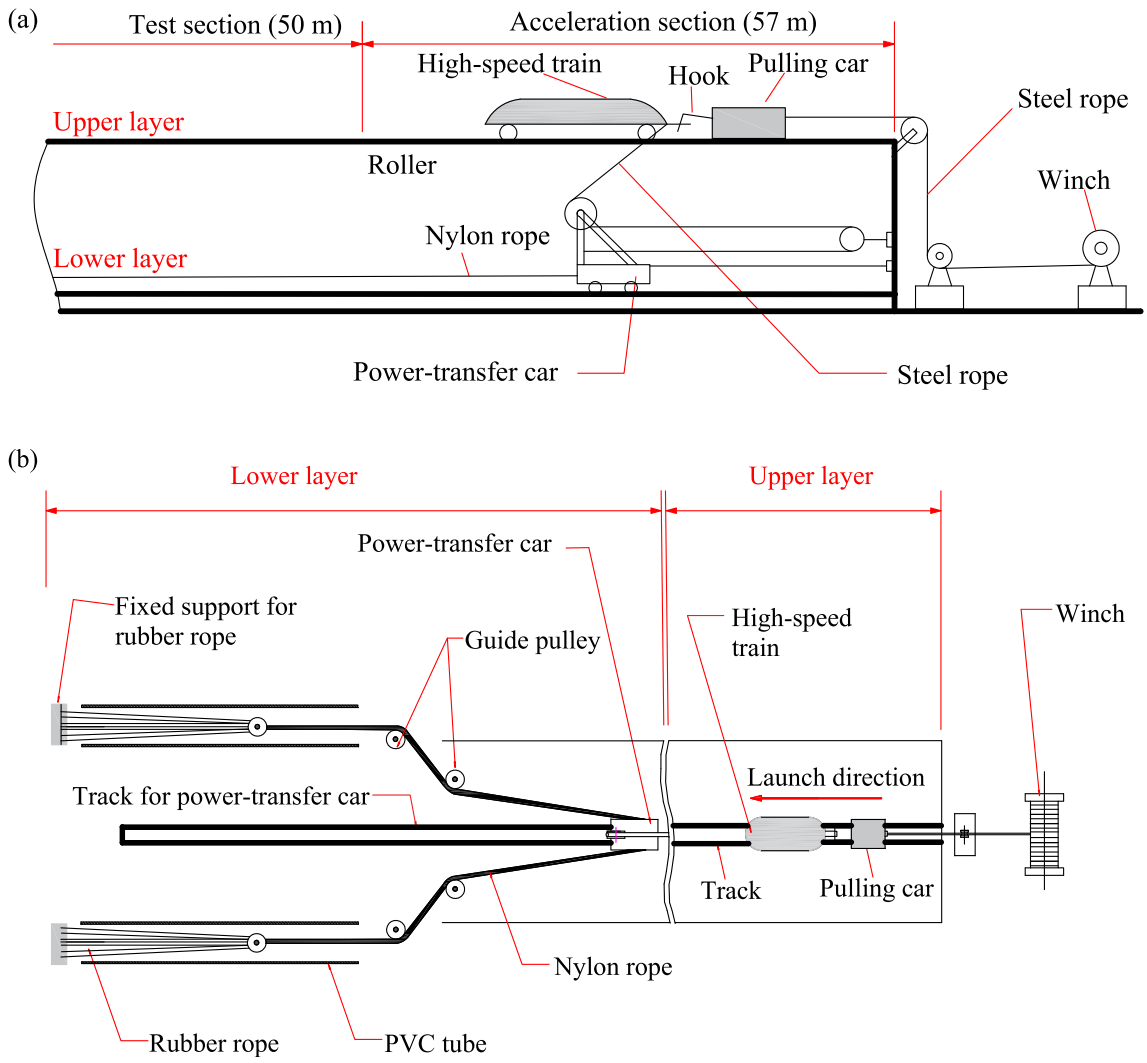

Fig. 2 Power system of the moving model rig: (a) side view of the upper layer; (b) top view.

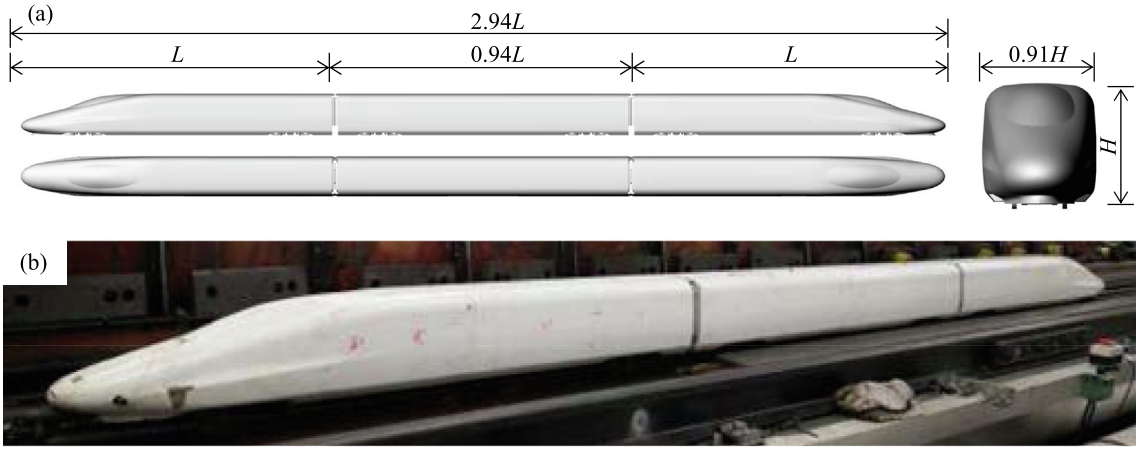

Fig. 3 High-speed train model: (a) geometric size; (b) photograph.

of the HST and (S=H = 0.22 m); and μ is the dynamic viscosity coefficient of air and $\mu = 18.2 \times 10^{-6}$N/m^2. According to Eq (1), the Reynolds number Re is larger than 1.03×10^6.

According to the European code [35], the Reynolds number has little effect on the aerodynamic characteristics of the train when two conditions are met: Firstly, the scale ratio of the experimental model should be larger than 1:25. Secondly, Re of the

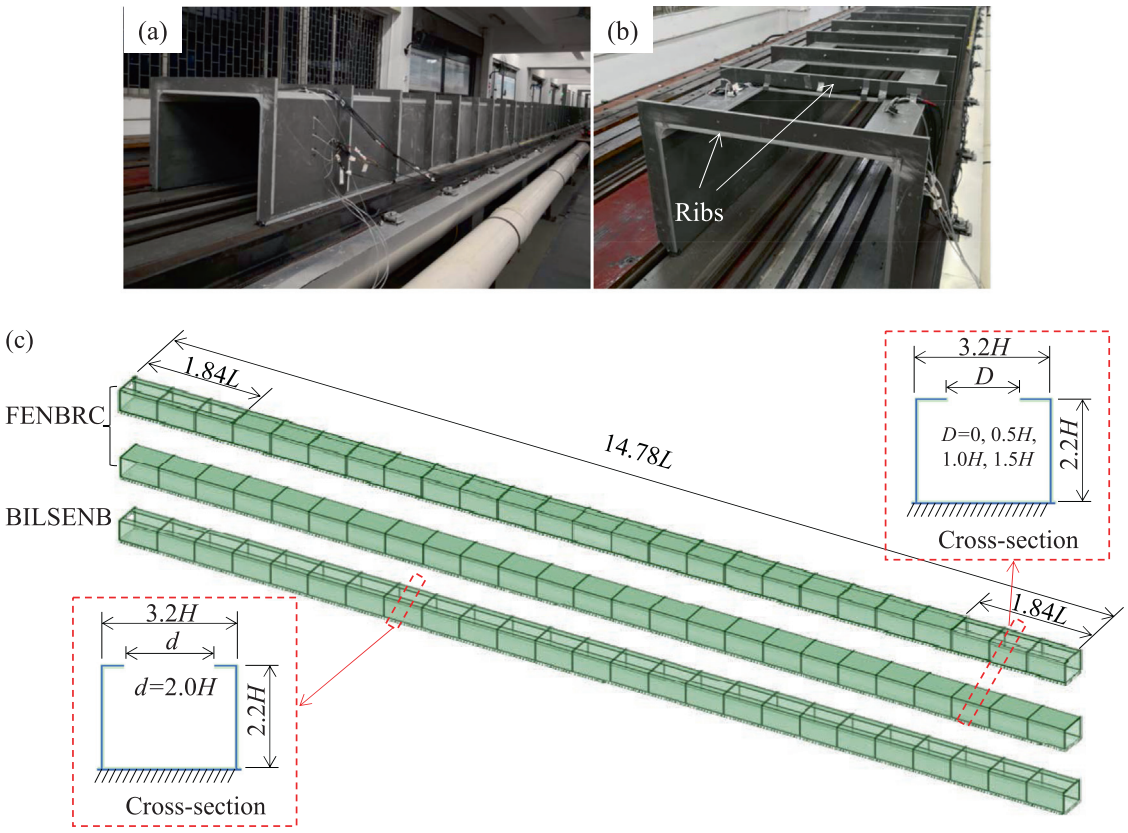

Fig. 4 City-oriented noise barrier model: (a) photograph of FENBRC; (b) photograph of BILSENB; (c) schematic view.

Table 2 Experiment case.

Case	Noise barrier type	Top opening	Train speed V (km/h)
1	FENBRC	$D = 0.5H$, $d = 0$	350
2		$D = 1.0H$, $d = 0$	350
3		$D = 1.5H$, $d = 0$	350
4		$D = 0$, $d = 0$	250
5		$D = 0$, $d = 0$	300
6		$D = 0$, $d = 0$	350
7	BILSENB	$D = 0$, $d = 2.0H$	250
8		$D = 0$, $d = 2.0H$	300
9		$D = 0$, $d = 2.0H$	350

experiment should be larger than Re_{cr} ($Re_{cr} = 3.6 \times 10^5$). The scale ratio of the current experiment is 1:16.8, which is perfectly satisfied with the first condition. Then, the characteristic height of the HST is normally regarded as the characteristic size, thus $S = 0.22$ m. The lowest speed of the HST in this research is 250 km/h. According to Eq. (1), Re of the current moving model experiment is greater than 1.08×10^6. Therefore, the second condition is met.

2.4. Data collection and processing

Fig. 5 shows the location of the measurement points arranged on the internal surface of all barrier models. Twenty-seven pressure measurement points is set on the noise barrier at nine sections (named as S1–S9). S1, S5 and S9 are defined as entrance, central and exit sections, respectively. The distance from S1 to entrance end and S9 to exit end is $0.36L$, and the distance of each section is $17.5L$. Seven measurement points are placed on the entrance, central and exit sections to understand the influence of circumferential position of measurement points on the transient pressure distribution. As shown in Fig. 5(b), taking S5 as an example, the measurement points are numbered in the counterclockwise direction. Measurement points S1-1, S1-2 and S1-3, with heights of $0.5H$, H and $1.6H$, are set on the side near the HST in sequence. Measurement points S1-4 and S1-5 are arranged on the roof and $0.5H$ and $2.7H$ from S1-1 horizontally. Measurement points S1-6 and S1-7, with heights of $2.7H$ and $0.5H$, respectively, are arranged on the far side of the HST.

The pressure data are collected by three types of equipment: *Honeywell DC030NDC4* micro differential pressure sensors, *NI CDAQ-9188* CompactDAQ Ethernet chassis and a computer with NI DAQmx driver and LabVIEW software. The *Honeywell DC030NDC4* is capable to run in a temperature of −25 °C-85 °C and outputs voltage of 0.25 V-4.25 V. The operating pressure and maximum pressure of Honeywell DC030NDC4 sensor are 7.48 kPa and 112.13 kPa, respectively. The micro differential pressure sensor records pressure data with a high sampling frequency of 5 kHz and a high accuracy of 2.5 %. As shown Fig. 6(a), the pressure sensor has two external channels testing the absolute pressure on the noise barrier surface and the environment reference pressure respectively. One channel is connected to the inner surface of the

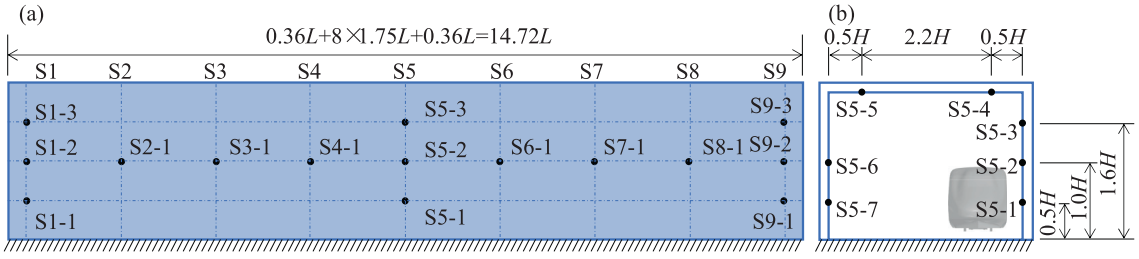

Fig. 5 Measurement point location: (a) side view; (b) cross section view of S5.

noise barrier using hoses with a diameter of 1.5 mm, and the other channel is extended to a stable atmospheric environment where the train wind has no influence on it. The difference of two channels is the actual pressure at the measurement point caused by the HST passing by. As shown Fig. 6(b), the *NI CDAQ-9188* is a four-module and eight-slot CompactDAQ Ethernet chassis which can integrate 16 sensors. In the current experiment, two *NI CDAQ-9188* chassis are combined with a network cable and collect the pressure data from 27 pressure sensors. Finally, the pressure data are uploaded to the local computer through Ethernet and is processed and stored.

The high-frequency components of the aerodynamic pressure have minor impacts on the noise barrier structure. Considering that the natural vibration frequencies of noise barriers are less than 20 Hz [19,36], the raw pressure data are filtered with a first-order low-pass Butterworth filter with a cut-off frequency of 20 Hz to reduce the disturbance of high-frequency components. Additionally, the pressure data are expressed as pressure coefficient C_p by Eq. (2) [35], and the time is expressed as nondimensionalised time $_t$ by Eq. (3):

$$C_p = \frac{P}{0.5\rho V^2} \tag{2}$$

$$t^* = tV/L \tag{3}$$

where P is the transient pressure collected by micro differential pressure sensors.

To facilitate the discussion, the pressure amplitude ΔP and coefficient of pressure amplitude ΔC_p are defined as Eqs. (4) and (5):

$$\Delta P = P_{\max} - P_{\min} \tag{4}$$

$$\Delta C_p = C_{p,\max} - C_{p,\min} \tag{5}$$

where P_{max} and P_{min} are positive and negative pressure peaks, respectively; and $C_{p,\max}$ and $C_{p,\min}$ are the coefficients of P_{max} and P_{min} calculated by Eq. (2), respectively.

2.5. Verification

In the moving model experiments, 15–20 repeated tests are needed to verify the data collection setup and the stability of the experimental model. When the error between the actual speed and the target speed of the repeated tests is above 2 %, the test data will be eliminated [30]. Cases 6 and 9 are typical cases of the HST passing through the noise barriers, and the corresponding train speed is 350 km/h. Fig. 7 shows the three closest repeated test results of measurement point S7–1 in the two cases. The time–history of the transient pressure obtained from three repeated tests is almost identical, with the maximum deviation less than 2 %, as shown in Fig. 7. Therefore, the results of the moving model experiment are reliable.

To validate the experimental results, we have tested the aerodynamic pressure of a traditional vertical noise barrier when high-speed train passes by, as shown in Fig. 8. The measurement arrangement is consistent with that shown in Fig. 5. As shown in Fig. 9(a), the field measurement of a vertical noise barrier in [19] is adopted here for verification. In [19], the train type is CRH380A, which is consistent with our research. Four train speeds, namely, 250 km/h, 300 km/h, 350 km/h, and 380 km/h, are tested in the field measurement. Fig. 9(b) shows the measurement point arrangement in [19].

The relative vertical position of measurement point 2 in Fig. 9(b) and S5-2 in Fig. 5 are close and the bottom area is insusceptible to the outer atmosphere. Therefore, the pressure time-histories of the two measurement points when the train speed is 350 km/h are compared in Fig. 10(a). The pressure time-history of the field measurement is also nondimensionalized by using Eqs. (2) and (3). It is worth noting that the CRH380A train in [19] has 16 carriages, which is different from that applied in this experiment. Consequently, only the head pulses are compared here. As shown in Fig. 10(a), the pressure variation of the head pulse in the filed measurement

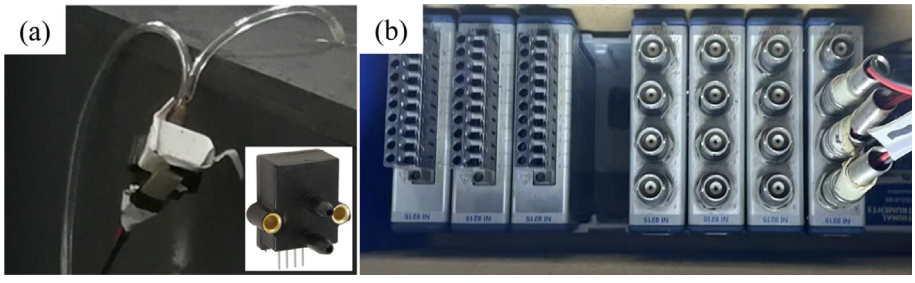

Fig. 6 Data collection equipment.

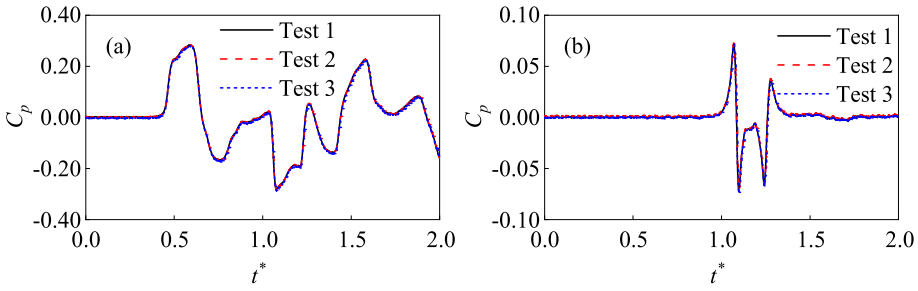

Fig. 7 Repeatability experiments of measuring point 7–1: (a) Case 6; (b) Case 9.

Fig. 8 The vertical noise barrier.

and the experiment are consistent. The peak pressure of the filed measurement is slightly lower than that of the experiment. A maximum difference between the two positive peaks is only 6 %. Moreover, ΔC_p of the section S5 (Fig. 5) and all the measurement points shown in Fig. 9(b) are further compared, as shown in Fig. 10(b). In this figure, the position of measurement points is presented by the normalized height of the noise barrier. As illustrated in Fig. 10(b), the values of ΔC_p in the experiment are slightly larger than those in the field measurement. However, the value of ΔC_p in the experiment and field measurement shows a same distribution rule, namely, decreasing with the increasing in the hight of measurement points. It is also worth mentioning that the two set of ΔC_p values are close, indicating that the experimental results are credible.

3. Results analysis and discussion

3.1. Transient pressure characteristics on FENBRC

To study the transient pressure characteristics on FENBRC, Fig. 11 shows the pressure time–histories of measurement point S5-2 in FENBRC$_{(D=0,\ d=0)}$ (Case 6). The typical pressure variation moments are marked by a1–a7 in the figure.

In Fig. 11, a significant piston effect presents when the HST passes through. When the train nose of the head carriage arriving the barrier, the static air in front of the train is instantly compressed by the impact of the HST, and the initial compression wave C1 is generated. When the tail nose runs in the noise barrier completely, the air cannot replenish the space originally occupied by the train, resulting in the initial expansion wave E1. The initial compression wave C1 and the initial expansion wave E1 propagate longitudinally at the sonic speed in the noise barrier. When the compression wave S1 reaches the measurement point S5-2 (a1), the pressure rapidly rises to $C_{p,\max}$. When the initial expansion wave E1 reaches the measurement point S5-2 (a2), the pressure begins to decrease. When the compression wave C1 reaches the exit of the noise barrier, a small part of the compression wave flows out of the exit in the form of micro pressure wave, and the rest of the compression wave is reflected into the noise barrier in the form of expansion wave E2. When the expansion wave E2 reaches the measurement point S5-2 (a3), the pressure further decreases. Then, the train arrives at the measurement point S5-2 (a4), and the positive pressure area at the nose tip slows down the pressure curve's decline rate slightly, while the negative pressure of the HST sharply increases the pressure decline rate, and the pressure rapidly decreases to $C_{p,\min}$. Expansion wave E1 propagates to the noise barrier exit and is reflected to form compression wave $C2$. When $C2$ reaches measurement

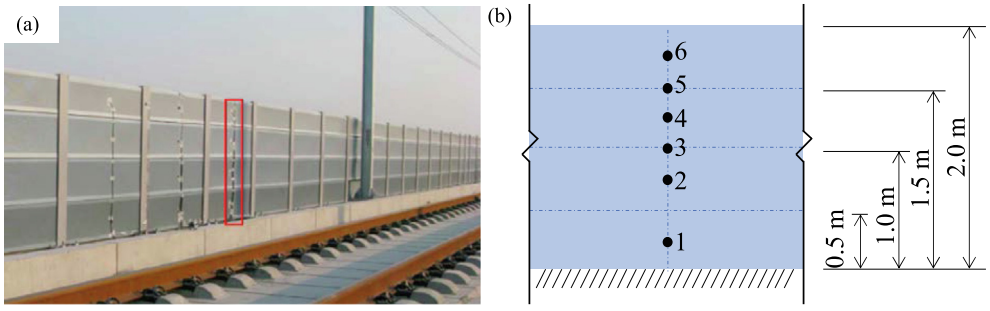

Fig. 9 Field measurement of [19]: (a) noise barrier; (b) measuring point arrangement.

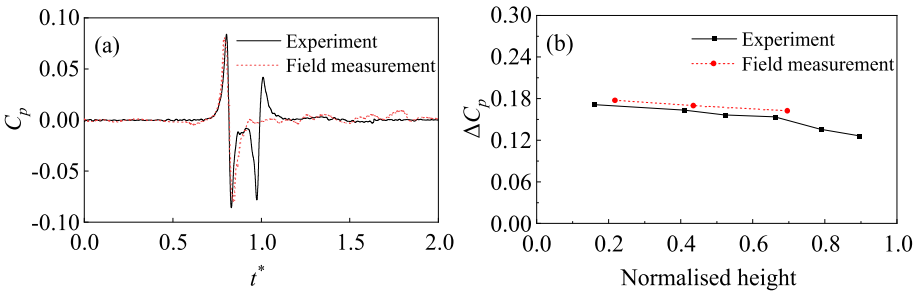

Fig. 10 Comparison between the experiment and field measurement: (a) head pulses; (b) ΔC_p values.

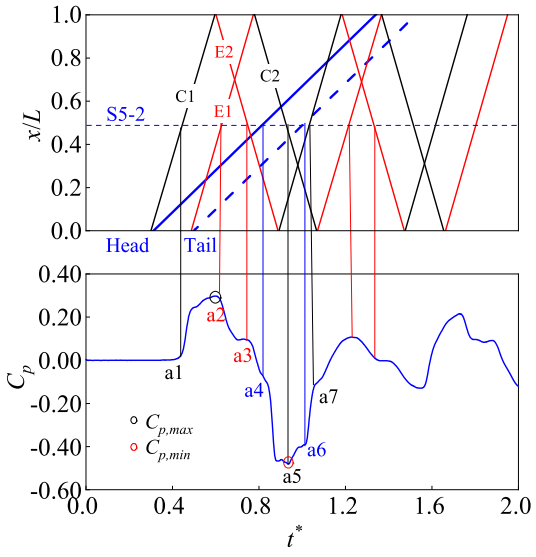

Fig. 11 Pressure propagation in the FENBRC$_{(D=0,\ d=2.0H)}$.

point S5-2 (a5), the pressure begins to rise. When the tail carriage reaches measurement point S5-2 (a6), the positive pressure area of the tail carriage causes the pressure to quickly rise. Thereafter, the compression and expansion wave reflect in the FENBRC$_{(D=0,\ d=0)}$, and the pressure value caused by the wave continues fluctuating. However, because the intensity of compression and expansion wave gradually decays in the propagation process, the positive and negative pressure at the subsequent pressure peaks can no longer exceed $C_{p,\max}$ or $C_{p,\min}$, respectively. It should be noticed that the application of the HST model with three carriages, instead of eight or 16, has a certain influence on the pressure propagation. For example, the reduction of carriage numbers generates an early initial expansion wave E1 (a2). Then, the compression wave $C2$ also shows ahead of time.

In summary, the pressure fluctuation in FENBRC$_{(D=0,\ d=0)}$ is mainly caused by two reasons: (1) Pressure field around the HST; (2) Propagation of pressure waves. The positive pressure peak is usually induced by the initial compression wave. The negative pressure peak is caused by the coupling of expansion wave and pressure field around the HST. The negative pressure peak can exceed the positive pressure peak by two times.

Fig. 12 compares the time–histories of transient pressure (S1-2, S5-2 and S9-2) in Cases 2 and 6 to demonstrate the influencing law of the top openings at the entrance and exit of the FENBRC on the pressure fluctuating law. Cases 2 and 6 are cases of FENBRC$_{(D=1.0H,\ d=0)}$ and FENBRC$_{(D=0,\ d=0)}$, respectively. In Fig. 12, the pressure fluctuation of the two noise barriers is basically identical, indicating that the top opening at the entrance and exit of the FENBRC has a weak influence on the propagation law of the internal pressure wave. As shown in Fig. 12(b), for the central section S5, the arrival time of the initial compression wave in the two cases is basically the same, causing the pressure to synchronously rise, and the pressure peaks of the two cases are almost equal. However, the pressure variation of FENBRC$_{(D=1.0H,\ d=0)}$ is slightly advanced with time, and the time lag between the pressure variation of the two noise barriers gradually increases. The reason is as follows: The formation and reflection positions of pressure waves in FENBRC$_{(D=0,\ d=0)}$ are at the ends of barriers, whereas in FENBRC$_{(D=1.0H,\ d=0)}$, the formation and reflection positions of pressure waves are in the opening section of the entrance and exit. The propagation way of pressure waves in FENBRC$_{(D=1.0H,\ d=0)}$ is shortened compared with FENBRC$_{(D=0,\ d=0)}$. As shown in Fig. 12(a) and (c), the top opening at the entrance and exit of the FENBRC$_{(D=1.0H,\ d=0)}$ has a pressure relief effect on the entrance and exit sections. The corresponding ΔC_p values of measurement points S1-2 and S9-2 decrease by 20.8 % and 29.2 %, respectively, with the top opening at the entrance and exit, whereas the pressure peak and amplitude of the middle measurement point are almost unaffected.

Fig. 13 shows and Table 3 summarises the longitudinal distribution of the pressure coefficient of pressure peaks and amplitude of FENBRC$_{(D=0,\ d=0)}$, FENBRC$_{(D=0.5H,\ d=0)}$, FENBRC$_{(D=1.0H,\ d=0)}$ and FENBRC$_{(D=1.5H,\ d=0)}$. The results of the nine measurement points with the height H are ploted in the figure, and the four cases corresponding to four different opening widths are Cases 6, 1, 2 and 3. Fig. 14 shows and Table 4 summarises the circumferential distribution of pressure coefficient of the pressure peaks and amplitude of the measurement points on S1, S5 and S9 sections in the four cases. The abscissa value in the figure represents the number of measurement points on each section. The $C_{p,\max}$ and $C_{p,\min}$ values refer to the left ordinate, and ΔC_p values refer to the right ordinate.

Fig. 13 and Table 3 demonstrates that:

(1) The $C_{p,\max}$, $C_{p,\min}$ and ΔC_p values of FENBRCs are small at two ends and large in the middle longitudinally. This is because sections S1 and S9 are close to the external atmosphere, and the compression and expansion wave is difficult to affect the pressure. Additionally, the $C_{p,\max}$ value of the S2 section is the largest, which is 27.8 % higher than the aver-

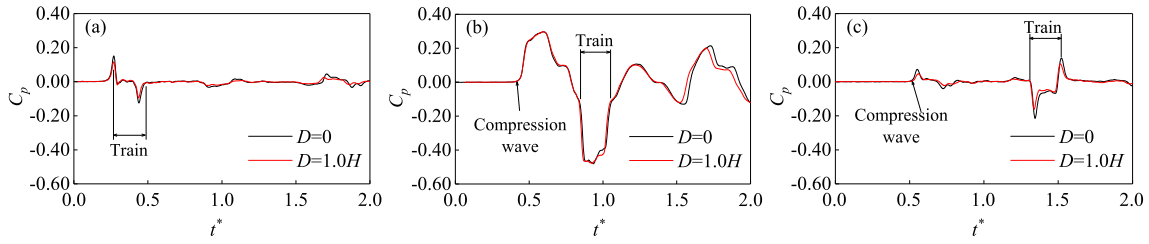

Fig. 12 Comparison of the pressure time–history between $\text{FENBRC}_{(D=0,\ d=0)}$ and $\text{FENBRC}_{(D=1.0H,\ d=0)}$: (a) S1-2; (b) S5-2; (c) S9-2.

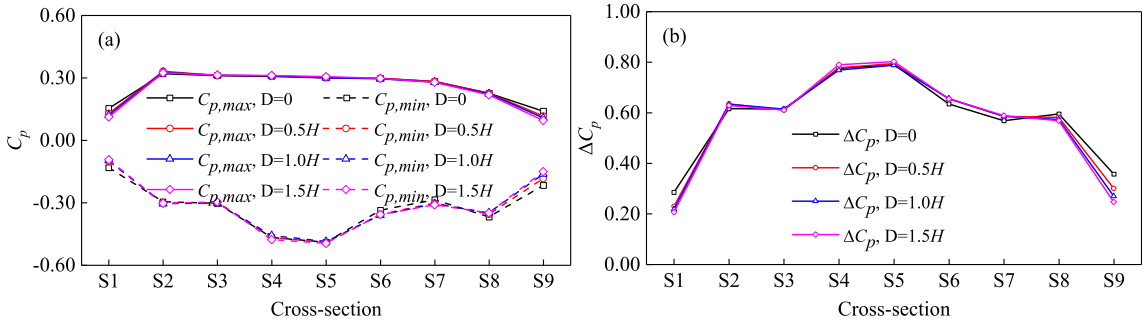

Fig. 13 Influence of the top opening width on the longitudinal pressure distribution inside the FENBRC.

Table 3 Pressure peaks and amplitudes along longitudinal direction under different top opening widths.

Cross-section	$D = 0$			$D = 0.5H$			$D = 1.0H$			$D = 1.5H$		
	$C_{p,\max}$	$C_{p,\min}$	ΔC_p	$C_{p,\max}$	$C_{p,\min}$	ΔC_p	$C_{p,\max}$	$C_{p,\min}$	ΔC_p	$C_{p,\max}$	$C_{p,\min}$	ΔC_p
S1	0.15	−0.13	0.29	0.13	−0.10	0.23	0.12	−0.10	0.22	0.11	−0.09	0.21
S2	0.32	−0.30	0.62	0.33	−0.30	0.63	0.33	−0.31	0.63	0.33	−0.30	0.63
S3	0.31	−0.30	0.61	0.31	−0.30	0.61	0.31	−0.30	0.61	0.31	−0.30	0.61
S4	0.31	−0.47	0.78	0.31	−0.47	0.78	0.31	−0.46	0.77	0.31	−0.48	0.79
S5	0.30	−0.49	0.79	0.30	−0.49	0.79	0.30	−0.49	0.79	0.31	−0.50	0.80
S6	0.30	−0.34	0.63	0.30	−0.36	0.65	0.30	−0.36	0.66	0.30	−0.36	0.65
S7	0.28	−0.29	0.57	0.28	−0.30	0.59	0.28	−0.31	0.59	0.28	−0.31	0.59
S8	0.23	−0.37	0.59	0.23	−0.36	0.58	0.22	−0.35	0.57	0.22	−0.35	0.57
S9	0.14	−0.22	0.36	0.12	−0.18	0.30	0.11	−0.16	0.27	0.10	−0.15	0.25

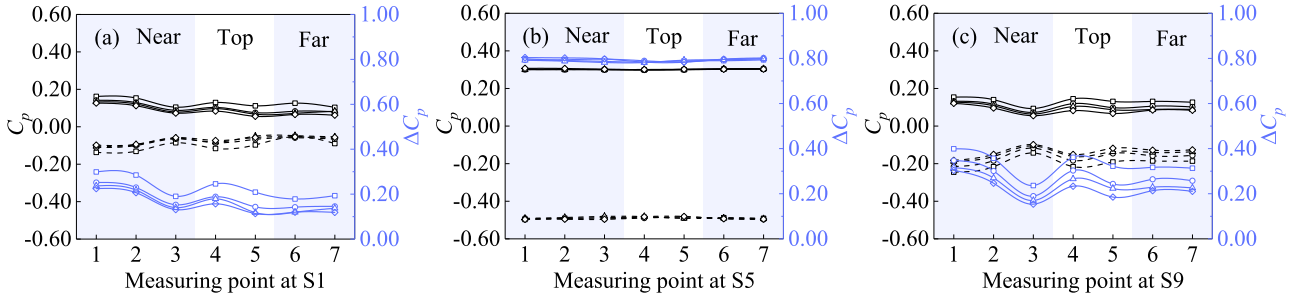

Fig. 14 Influence of the top opening width on the circumferential pressure distribution inside the FENBRC: (a) cross-section S1; (b) cross-section S5; (c) cross-section S9.

age $C_{p,\max}$ value of the nine measurement points This is because the pressure attenuates after S2 section when propogating in the noise barrier. The $C_{p,\min}$ and ΔC_p values of the S4 and S5 sections are 55.0 % and 38.7 % higher than the average values of the nine measurement points, respectively, because of the coupling effect of the expansion wave and negative pressure area around the HST.

(2) When the opening width at the entrance and exit changes, the pressure variation range of the FENBRC has a nonlinear relation with opening widths. When the open

Table 4 Pressure peaks and amplitudes along circumferential direction under different top opening widths.

Point	$D = 0$			$D = 0.5H$			$D = 1.0H$			$D = 1.5H$		
	$C_{p,\max}$	$C_{p,\min}$	ΔC_p	$C_{p,\max}$	$C_{p,\min}$	ΔC_p	$C_{p,\max}$	$C_{p,\min}$	ΔC_p	$C_{p,\max}$	$C_{p,\min}$	ΔC_p
S1-1	0.16	−0.14	0.30	0.14	−0.11	0.25	0.13	−0.10	0.24	0.13	−0.10	0.22
S1-2	0.15	−0.13	0.29	0.13	−0.10	0.23	0.12	−0.10	0.22	0.11	−0.09	0.21
S1-3	0.10	−0.09	0.19	0.09	−0.06	0.15	0.08	−0.06	0.14	0.07	−0.06	0.13
S1-4	0.13	−0.12	0.25	0.10	−0.09	0.19	0.10	−0.08	0.18	0.08	−0.07	0.16
S1-5	0.11	−0.10	0.21	0.08	−0.07	0.14	0.07	−0.05	0.12	0.06	−0.06	0.11
S1-6	0.13	−0.05	0.18	0.08	−0.06	0.14	0.07	−0.05	0.12	0.07	−0.05	0.12
S1-7	0.10	−0.09	0.19	0.08	−0.07	0.15	0.08	−0.05	0.14	0.06	−0.06	0.12
S5-1	0.30	−0.50	0.80	0.30	−0.49	0.79	0.30	−0.49	0.79	0.31	−0.50	0.80
S5-2	0.30	−0.49	0.79	0.30	−0.49	0.79	0.30	−0.49	0.79	0.31	−0.50	0.80
S5-3	0.30	−0.49	0.79	0.30	−0.49	0.80	0.30	−0.48	0.78	0.30	−0.50	0.80
S5-4	0.30	−0.49	0.78	0.30	−0.49	0.79	0.30	−0.48	0.78	0.30	−0.48	0.78
S5-5	0.30	−0.49	0.79	0.30	−0.48	0.78	0.30	−0.49	0.79	0.30	−0.48	0.78
S5-6	0.30	−0.49	0.79	0.30	−0.49	0.80	0.30	−0.49	0.79	0.30	−0.49	0.80
S5-7	0.30	−0.49	0.79	0.31	−0.50	0.80	0.30	−0.49	0.80	0.30	−0.50	0.80
S9-1	0.15	−0.25	0.40	0.13	−0.22	0.35	0.13	−0.19	0.32	0.12	−0.18	0.30
S9-2	0.14	−0.22	0.36	0.12	−0.18	0.30	0.11	−0.16	0.27	0.10	−0.15	0.25
S9-3	0.09	−0.14	0.24	0.07	−0.12	0.19	0.06	−0.11	0.17	0.06	−0.10	0.15
S9-4	0.15	−0.22	0.36	0.12	−0.18	0.30	0.10	−0.16	0.27	0.08	−0.15	0.23
S9-5	0.13	−0.19	0.32	0.10	−0.15	0.24	0.09	−0.14	0.22	0.07	−0.12	0.19
S9-6	0.13	−0.19	0.32	0.11	−0.16	0.26	0.09	−0.14	0.23	0.08	−0.13	0.21
S9-7	0.13	−0.19	0.31	0.10	−0.16	0.26	0.09	−0.14	0.23	0.08	−0.13	0.21

increases from 0 to $0.5H$, $C_{p,\max}$ and $C_{p,\min}$ of the S1 section decrease by 15.9 % and 23.6 %, respectively, and ΔC_p decreases by 19.5 %. The $C_{p,\max}$ and $C_{p,\min}$ of the S9 section decrease by 16.9 % and 15.1 %, respectively, and ΔC_p decreased by 15.8 %. When the open increases from $1.0H$ to $1.5H$, the $C_{p,\max}$ and $C_{p,\min}$ of the S1 section decrease by 7.6 % and 2.4 %, respectively, and ΔC_p decreases by 5.3 %. The $C_{p,\max}$ and $C_{p,\min}$ of the S9 section decreased by 11.2 % and 7.0 %, respectively, and ΔC_p decreases by 15.8 %.

Fig. 14 and Table 4 demonstrates that: the pressure of the S1 and S9 sections significantly changes along the circumferential direction due to the influence of the top opening, and the specific distribution characteristic is as follows:

(1) The $C_{p,\max}$, $C_{p,\min}$ and ΔC_p values of the measurement points at the side near the HST decrease with the increase in height. In comparison with the measurement point at $0.5H$, the $C_{p,\max}$ values of the measurement points at $1.6H$ of the S1 and S9 sections are 38.9 % and 46.5 % lower, the $C_{p,\min}$ values are 40.0 % and 44.2 % lower, and the ΔC_p values are 39.4 % and 45.1 % lower, respectively. This result is obtained because the lower the measurement point is, the smaller the effective space of air flow is, and the greater the pressure is affected by the HST.

(2) With regard to the measurement point at the top of the noise barrier, the further away from the HST, the lower the pressure, i.e., the pressure value of the fourth measurement point is larger than that of the fifth. In comparison with the fifth measurement point, the $C_{p,\max}$ values of the fourth measurement point of the S1 and S9 sections are 33.2 % and 18.0 % higher, the $C_{p,\min}$ values are 30.5 % and 20.3 % higher, and the ΔC_p values are 32.0 % and 19.4 % higher, respectively.

(3) The distance between the two measurement points on the far side and the train surface is close, and the corresponding pressure values have no obvious difference. For the S5 section, the values of $C_{p,\max}$, $C_{p,\min}$ and ΔC_p are almost the same, indicating that the aerodynamic pressure of the middle sections of FENBRC has a one-dimension characteristic.

3.2. Comparison between FENBRC$_{(D=0,\ d=0)}$ and BILSENB$_{(D=0,\ d=2.0H)}$

3.2.1. Time-history and spatial characteristic of aerodynamic pressure

Taking the measurement point S5-2 in Case 9 as an example, Fig. 15 presents the typical transient pressure time–history of the BILSENB$_{(D=0,\ d=2.0H)}$. In this figure, the pressure time–history is composed of a head pulse, a tail pulse and stable sections. When the HST runs on the open line, a forward high-speed airflow is generated at the nose tip of the head carriage, the backward high-speed airflow is generated at the rear of the nose tip, and the air speed at the body is relatively low. The generation mechanism of the head pulse is as follows: The train head pushes the high-speed airflow to the inner surface of the noise barrier when arriving at the measurement point, and the impact effect of the airflow causes the pressure of the measurement point to rapidly rise to the positive peak. After the nose tip passes through the measurement point, the adsorption effect of the airflow causes the pressure to drop to the negative pressure peak. When the HST head passes through the measurement point, the wind speed near the train body is relatively stable, and the pressure curve gradually rises to the stable section, as indicated by circle 1. The pressure curve still fluctuates in a small range in the stable section due to the presence of gaps between each carriage (Fig. 3). This phenomenon has also been reported in other similar studies

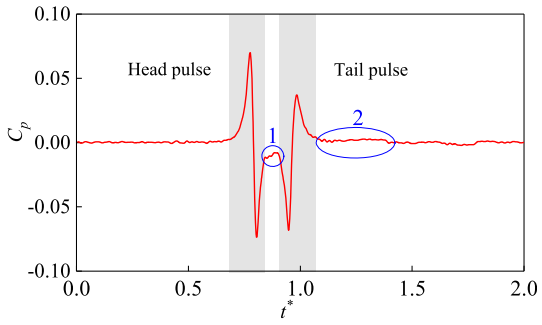

Fig. 15 Characteristic pressure curve of BILSENB$_{(D=0,\ d=2.0H)}$ (S5-2 of Case 9).

[31,37]. When the tail carriage passes the measurement point, the fluctuating law of the tail pulse is completely opposite to that of the head pulse. After the HST passes through, two reverse rotating vortexes are generated, resulting in more intense and complex flow field changes [7,26], thus causing more slight fluctuations in pressure curves, as indicated by circle 2. For the BILSENB$_{(D=0,\ d=2.0H)}$, the reduction of carriage numbers has no influence on the pressure amplitude of the head and tail pulse. This reduction only reduces the length of the stable section marked by circle 1.

In summary, the pressure fluctuation on the inner surface of the BILSENB$_{(D=0,\ d=2.0H)}$ is mainly caused by the impact and adsorption effect of the airflow caused by HST passing by. The pressure of BILSENB$_{(D=0,\ d=2.0H)}$ is more significantly influenced by the HST head, and the amplitude of the head pulse is 36.67 % higher than that of the tail pulse.

Fig. 16 shows the comparison of the pressure time–histories of S1-2, S5-2 and S9-2 in FENBRC$_{(D=0,\ d=0)}$ and BILSENB$_{(D=0,\ d=2.0H)}$.

In Fig. 16, the pressure fluctuation of the FENBRC$_{(D=0,\ d=0)}$ is significantly greater than that of the BILSENB$_{(D=0,\ d=2.0H)}$. As shown in Fig. 16(a) and (c), $C_{p,\max}$, $C_{p,\min}$ and ΔC_p of measurement point S1-2 of the FENBRC$_{(D=0,\ d=0)}$ are 68.0 %, 77.9 % and 72.4 % higher than those of the BILSENB$_{(D=0,\ d=2.0H)}$, respectively. $C_{p,\max}$, $C_{p,\min}$ and ΔC_p of S9-2 are 148.7 %, 210.8 % and 183.0 % higher than those of the BILSENB$_{(D=0,\ d=2.0H)}$, respectively. The reason maybe as follows: When the train arrives at the exit of the BILSENB$_{(D=0,\ d=2.0H)}$, the high-speed air in front of the nose tip is more likely to leak through the top opening, weakening the impact or adsorption effect. As shown in Fig. 16(b), due to the coupling effect of the pressure wave inside FENBRC$_{(D=0,\ d=0)}$ and the pressure field of the train, $C_{p,\max}$, $C_{p,\min}$ and ΔC_p of measurement point S5-2 are 330.0 %, 561.2 % and 491.3 % higher than those of BILSENB$_{(D=0,\ d=2.0H)}$, respectively.

To further understand the difference in the spatial characteristic of the transient pressure of FENBRC$_{(D=0,\ d=0)}$ and BILSENB$_{(D=0,\ d=2.0H)}$, Fig. 17 shows the the peak value and amplitude of pressure coefficient of nine longitudinal measurement points near the HST side with height H in FENBRC$_{(D=0,\ d=0)}$ and BILSENB$_{(D=0,\ d=2.0H)}$. Taking the central section S5 as an example, Fig. 18 shows the comparison of the pressure time–histories of four circumferential points on the S5 section under Cases 6 and 9. Fig. 19 shows the circumferential distribution of the peak value and amplitude of the pressure coefficient.

Fig. 17 depicts that:

(1) The pressure peak and amplitude of the BILSENB$_{(D=0,\ d=2.0H)}$ are significantly lower than those of the FENBRC$_{(D=0,\ d=0)}$. The average values of $C_{p,\max}$, $C_{p,\min}$ and ΔC_p of the nine measurement points at H are 362.8 %, 338.4 and 301.1 % higher than those of the BILSENB$_{(D=0,\ d=2.0H)}$, respectively.

(2) The aerodynamic pressure of the FENBRC$_{(D=0,\ d=0)}$ presents a non-uniform distribution characteristic longitudianlly of small at two ends and large in the middle. The $C_{p,\max}$, $C_{p,\min}$ and ΔC_p values of the central section S5 are 13.4 %, 34.4 % and 26.4 % higher than the averages of nine points, respectively. However, the longitudinal pressure of the BILSENB$_{(D=0,\ d=2.0H)}$ has an end effect, i.e., the value of the S2-S8 section does not change with the longitudinal position of measurement points, and only a slight deviation at the entrance and exit section of the noise barrier is observed. The $C_{p,\max}$ and ΔC_p values of the S1 section are 28.7 % and 14.1 % higher than the averages of S2–S8 sections, respectively. The $C_{p,\max}$ and ΔC_p values of the S9 section are 20.6 % and 12.9 % lower than the averages of S2–S8, respectively. The reasons may be as follows: When approaching the entrance section, the HST suddenly enters a semi-enclosed environment, and the high-speed air in front of the HST cannot flow around instantly. Hence, the difference between the airflow speed at the train head and that at the entrance section is high, resulting in a more significant airflow impact effect on the entrance section than on the middle sections. However, the high-speed air simultaneously flows out through two channels before the train arrives at the exit section, i.e., the top and exit of the noise barrier. The difference between the airflow speed at the train head and that at the exit section is low, thus weakening the airflow impact effect.

Figs. 18 and 19 indicate that:

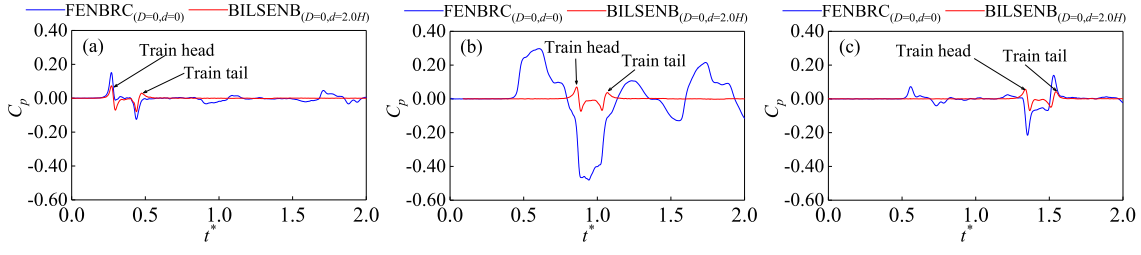

Fig. 16 Comparison of pressure time–history between FENBRC$_{(D=0,\ d=0)}$ and BILSENB$_{(D=0,\ d=2.0H)}$ (Cases 6 and 9): (a) S1-2; (b) S5-2; (c) S9-2.

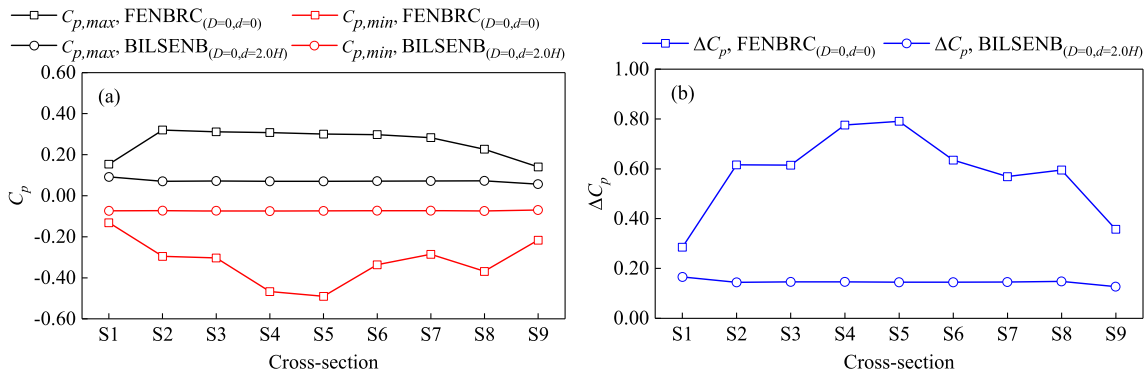

Fig. 17 Comparison of the longitudinal pressure distribution between FENBRC$_{(D=0,\ d=0)}$ and BILSENB$_{(D=0,\ d=2.0H)}$ (Cases 6 and 9): (a) $C_{p,\max}$ and $C_{p,\min}$; (b) ΔC_p.

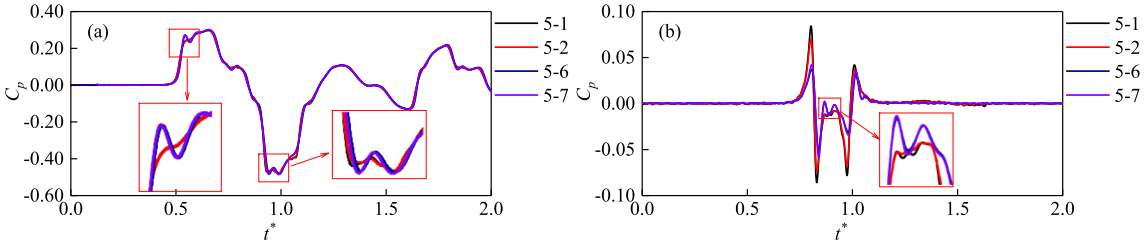

Fig. 18 Circumferential distribution of the pressure time–history at S5 of FENBRC$_{(D=0,\ d=0)}$ and BILSENB$_{(D=0,\ d=2.0H)}$ (Cases 6 and 9).

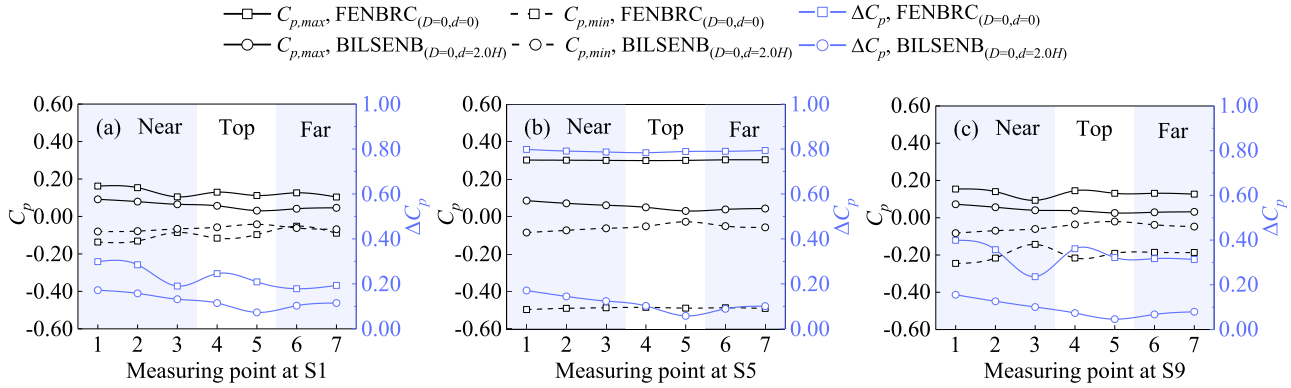

Fig. 19 Comparison of the circumferential pressure distribution between FENBRC$_{(D=0,\ d=0)}$ and BILSENB$_{(D=0,\ d=2.0H)}$ (Cases 6 and 9).

(1) For the central section of the FENBRC$_{(D=0,\ d=0)}$, the pressure time–history of the measurement points at the same section is basically identical, and the pressure peak and amplitude are almost the same. This phenomenon again confirms that the compression and expansion wave have significant one-dimensional characteristics when propagating in the FENBRC$_{(D=0,\ d=0)}$. Notably, the fluctuating law of pressure at points S5-6 and S5-7 on the far side of the HST are slightly different from those of measurement points S5-1 and S5-2 on the symmetrical position near the HST side, which is similar to the transient pressure in the tunnel reported by Zhang et al. [20]. The reason may be as follows: The influence of the pressure wave and pressure field around the train on far measurement points is smaller than the near measurement points, resulting in the pressure time–history curve shows a small fluctuating similar to a harmonic wave.

(2) For the BILSENB$_{(D=0,\ d=2.0H)}$, the pressure time–histories of measurement points at different circumferential positions are basically consistent. When the train body passes, S5-6 and S5-7 also show pressure fluctuations similar to harmonics. The pressure of the three typical sections of the BILSENB$_{(D=0,\ d=2.0H)}$ has the following relationship with the circumferential position of the measurement points: The pressure of the measurement points on the side near the HST decreases with the increase in measurement point height. When the measurement height increases from $0.5H$ to $1.6H$, $C_{p,\max}$ of the S1, S5 and S9 decreases by 29.1 %, 29.0 % and 44.8 %, $C_{p,\min}$ decreases by 17.1 %, 26.1 % and 17.0 %, and

ΔC_p decreases by 15.5 %, 27.5 % and 35.3 %, respectively. Accordingly, the area at the bottom of the noise barrier should be highly concerned in design when applying the BILSENB$_{(D=0,\ d=2.0H)}$ to practical engineering. In terms of the measurement points at the top, for S1, S5 and S9, ΔC_p values of the fourth point are 36.4 %, 43.4 % and 37.5 % higher than those of the fifth, respectively. With regard to the measurement points on the far side, ΔC_p values of the seventh measurement point of the S1, S5 and S9 are 11.5 %, 13.3 % and 17.7 % higher than those of the sixth, respectively.

3.2.2. Train speed effect

To reveal the difference in the influence law of the HST speed on the transient pressure of the FENBRC$_{(D=0,\ d=0)}$ and BILSENB$_{(D=0,\ d=2.0H)}$, Fig. 20 presents the transient pressure time–histories of measurement points S1-2, S5-2 and S9-2 in Cases 4 to 9. The noise barrier type of Cases 4 to 6 is FENBRC$_{(D=0,\ d=0)}$, and that of Cases 7 to 9 is BILSENB$_{(D=0,\ d=2.0H)}$. The HST passes through the FENBRC$_{(D=0,\ d=0)}$ and BILSENB$_{(D=0,\ d=2.0H)}$ at a speed of 250 to 350 km/h, respectively.

Fig. 20 demonstrates that: (1) For sections S1 and S9 of the FENBRC$_{(D=0,\ d=0)}$, the pressure fluctuating law is basically identical under different train speeds, and the coefficient of pressure peaks caused by train passing by is close. For the central section S5, under different train speeds, the dimensionless peak of the initial compression wave is basically the same, and the dimensionless time for the HST to arrive at the measurement point is the same. However, because of the complex coupling effect of the pressure wave and pressure field around the HST, the peak values of negative pressure greatly vary with train speeds. In addition, the pressure fluctuation law shows significant differences under different train speeds. The reason is that pressure waves are propagating at a constant speed inside the noise barrier, whereas the train speed varies. When the time is nondimensionalised by Eq. (3), the dimensionless time of the HST arriving at the measurement point remains unchanged under different train speeds, whereas the dimensionless time of the pressure waves arriving at the measurement point varies. (2) For the BILSENB$_{(D=0,\ d=2.0H)}$, the pressure fluctuating law under different train speeds is in good agreement, and the pressure peaks are basically the same. The results indicating that the dimensionless method adopted in this research is reasonable and further confirms the feasibility of extending the moving model results to the engineering practices.

To obtain a quantitative law between the HST speed and transient pressure of the two types of FENBRC$_{(D=0,\ d=0)}$ and BILSENB$_{(D=0,\ d=2.0H)}$, the positive peak P_{max}, negative peak P_{min} and amplitude ΔP of the nine same height points at the FENBRC$_{(D=0,\ d=0)}$ and BILSENB$_{(D=0,\ d=2.0H)}$ are shown in Fig. 19 under different train speeds.

In Fig. 21: (1) In the FENBRC$_{(D=0,\ d=0)}$, P_{max}, P_{min} and ΔP of each measurement point at different train speeds basically meet the law of small at two ends and large in the middle. However, the negative pressure peak of the S5 section is lower than that of adjacent sections when the train speed is 250 km/h, which is caused by the inconsistency between the arrival time of the expansion wave and the negative pressure area of the HST at the S5 section (Fig. 20 (a_2)). When the HST velocity increased from 250 to 350 km/h, the P_{max} and P_{min} values of the FENBRC$_{(D=0,\ d=0)}$ increased by 100.4 % and 95.2 % on average, and ΔP increased by 97.5 % on average. (2) For the BILSENB$_{(D=0,\ d=2.0H)}$, the longitudinal pressure distribution law under different train speeds is similar. The P_{max} and P_{min} values of the BILSENB$_{(D=0,\ d=2.0H)}$ increased by 109.1 % and 111.9 % on average, respectively, and ΔP increased by 110.1 % on average.

A quantitative analysis is performed here by curve fittings. The power function is adopted here to fit the relationship between the train speed and aerodynamic pressure. The train speed V is taken as the independent variable, and the power law is adopted to fit P_{max}, P_{min} and ΔP with the train speed V, as expressed in Eq. (6):

$$P = aV^b \tag{6}$$

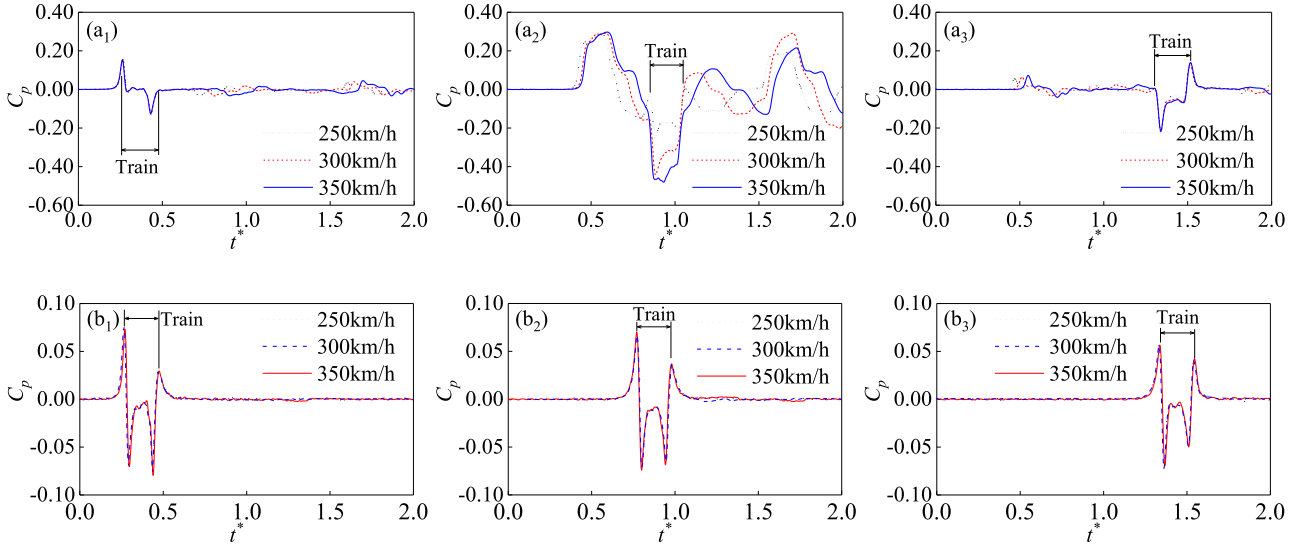

Fig. 20 Influence of train speed on pressure time–history: (a_1–a_3) S1-2, S5-2 and S9-2 of FENBRC$_{(D=0,\ d=0)}$; (b_1–b_3) S1-2, S5-2 and S9-2 of BILSENB$_{(D=0,\ d=2.0H)}$.

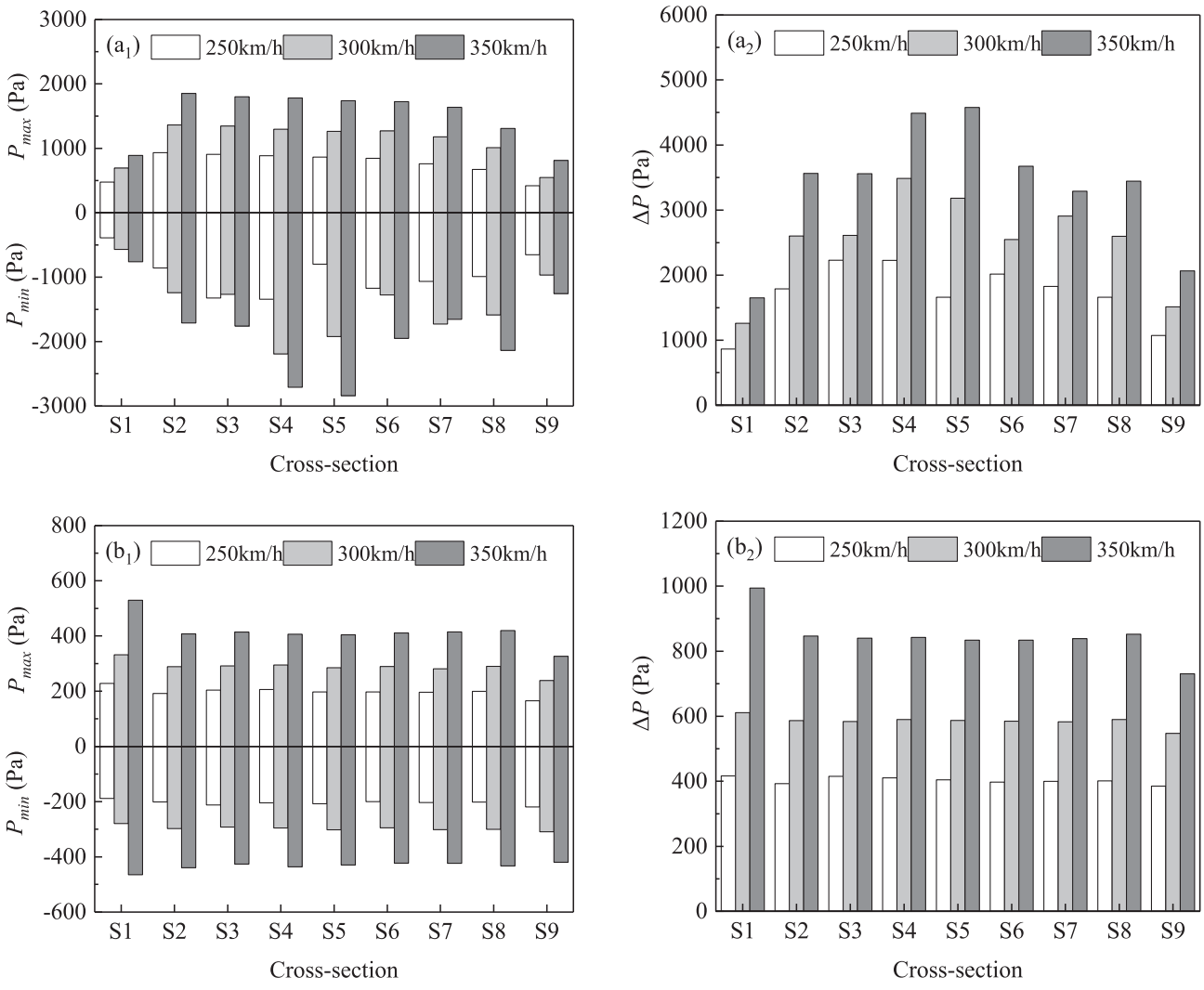

Fig. 21 Influence of train speed on the pressure peak and amplitude: (a_1) P_{max} and P_{min} of FENBRC$_{(D=0,\ d=0)}$; (a_2) ΔP of FENBRC$_{(D=0,\ d=0)}$; (b_1) P_{max} and P_{min} of BILSENB$_{(D=0,\ d=2.0H)}$; (b_2) ΔP of BILSENB$_{(D=0,\ d=2.0H)}$.

where P is the pressure obtained in the experiment and is equal to P_{max}, P_{min} and ΔP in this subsection; and a and b are fitted constants.

The relationship between C_p and HST speed V is expressed by substituting Eq. (2) into Eq. (6):

$$C_p = \frac{2a}{\rho} V^{b-2} \tag{7}$$

Fig. 22 shows the fitting results of the nine same height measurement points, and Table 5 summarises the corresponding fitting parameters. The reliability of a curve fitting is determined by two factors, namely, the fitting function and determination coefficient R^2. Firstly, the power function function is domonstrated to be capable for describing the relationship between the train speeds and corresponding aerodynamic impacts [7,19,20]. Hence, the power function is deemed to be an appropriate function to be applied here. Secondly, as listed in Table 5, for the FENBRC$_{(D=0,\ d=0)}$, the determination coefficient R^2 of all the fitting curve for P_{max} is greater than 0.95. For the BILSENB$_{(D=0,\ d=2.0H)}$, the R^2 of all fitted lines are larger than 0.95. Therefore, the fitting results are deemed to be reliable.

According to Fig. 22 and Table 5:

(1) For the FENBRC$_{(D=0,\ d=0)}$, the determination coefficient R^2 of all the fitting curve for P_{max} is greater than 0.95, indicating that the fitting results are reliable. The index b is approximately-two. The impact of the initial compression wave is proportional to the quadratic power of the train speed because the P_{max} values of the FENBRC$_{(D=0,\ d=0)}$ are mainly induced by the initial compression wave. The negative pressure peaks P_{min} of measurement points S3-1, S6-1 and S7-1 significantly deviate from the power function relationship with the train speed (shown in bold in Table 5). Although P_{min} of measurement point S5-2 satisfies the power function relationship with the train speed, fitting parameter b reaches 3.31. According to the aforementioned analysis, the negative pressure peak P_{min} on the inner surface of the FENBRC$_{(D=0,\ d=0)}$ is caused by the coupling effect of the expansion wave and the negative pressure area of the train; thus, its relationship with the train speed is more complex. The P_{min} and ΔP values of the other measurement points basically meet the quadratic function relation with the train speed, except S3-1, S5-2, S6-1 and S7-1.

(2) For the BILSENB$_{(D=0,\ d=2.0H)}$, the R^2 of all fitted lines are larger than 0.95, showing that the relationship between

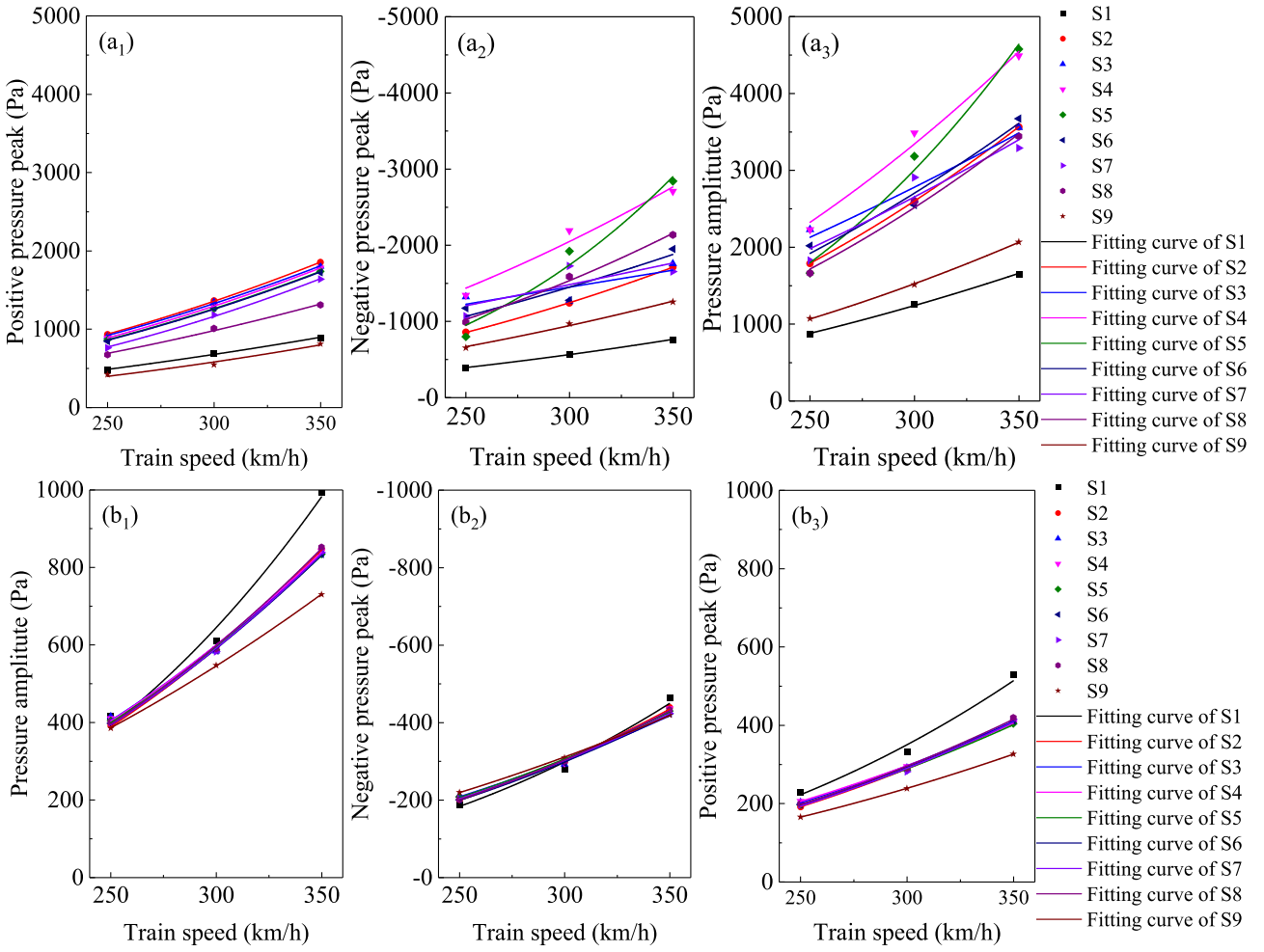

Fig. 22 Fitting results of the power function: (a_1–a_3) P_{max}, P_{min} and ΔP of FENBRC$_{(D=0,\ d=0)}$; (b_1–b_3) P_{max}, P_{min} and ΔP of BILSENB$_{(D=0,\ d=2.0H)}$.

P_{max}, P_{min} and ΔP of the BILSENB$_{(D=0,\ d=2.0H)}$ and the train speed well satisfies the power function relationship. From the perspective of the index b, the relationship P_{max}, P_{min} and ΔP of the BILSENB$_{(D=0,\ d=2.0H)}$ and the train speed still presents the end effect. Specifically, index b of the S1 section is significantly larger than that of the S2–S8 section, reaching a maximum of 2.73. Index b of the S9 section is smaller than that of S2–S8, and the minimum is only 1.90. This phenomenon reveals that the sensitivity of the pressure of the S1 section to speed is higher than those of the S2–S8 sections, while the sensitivity of the transient pressure of the S9 section to speed is lower than those of the S2–S8. It is worth noting that the index b of all sections except S9 are higher than two, and the mean values of P_{max}, P_{min} and ΔP of the S1–S8 sections are 2.20, 2.27 and 2.28, respectively. According to references [7,36], ΔP of vertical noise barriers is proportional to the square of HST velocity. Specifically, the internal pressure of the BILSENB$_{(D=0,\ d=2.0H)}$ is more susceptible to the HST velocity compared with vertical barriers.

(3) With regard to the fitting relationship between P_{max}, P_{min} and ΔP and the train speed, index b of the BILSENB$_{(D=0,\ d=2.0H)}$ is generally larger than that of the FENBRC$_{(D=0,\ d=0)}$. In terms of index b fitted by P_{max} and the train speed, the mean value of the BILSENB$_{(D=0,\ d=2.0H)}$ at the nine measurement points at the same height is 6.7 % higher than that of the FENBRC$_{(D=0,\ d=0)}$. Meanwhile, the mean values of the five measurement points on the BILSENB$_{(D=0,\ d=2.0H)}$ for index b fitted by P_{min} and ΔP with the train speed are 13.1 % and 13.9 % higher than the corresponding values of the FENBRC$_{(D=0,\ d=0)}$, except for measurement points S3-1, S5-2, S6-1 and S7-1. The reason is as follows: The transient pressure of the FENBRC$_{(D=0,\ d=0)}$ is influenced by the pressure wave and the pressure field around the train, whereas the transient pressure of the BILSENB$_{(D=0,\ d=2.0H)}$ is dominated by the train. Consequently, the transient pressure of the BILSENB$_{(D=0,\ d=2.0H)}$ is more sensitive to the train speed.

3.3. Spectral comparison of the transient aerodynamic pressure between the FENBRC$_{(D=0,\ d=0)}$ and BILSENB$_{(D=0,\ d=2.0H)}$

A sepctral analysis is conducted in this section to measure the level of aerodynamic impacts of train-induced pressure on different noise barriers in the frequency domian. Meanwhile, an understanding about the aerodynamic pressure in the frequency domain is also necessary to avoid the resonance effect and improve the performance of noise barriers. The fast

Table 5 Fitting parameters of the power function.

Point	Parameters	$FENBRC_{(D=0,\ d=0)}$			$BILSENB_{(D=0,\ d=2.0H)}$		
		P_{max}	P_{min}	ΔP	P_{max}	P_{min}	ΔP
S1-2	a	0.02	0.01	0.03	0.00	0.00	0.00
	b	1.82	1.97	1.89	2.49	2.66	2.73
	R^2	0.9948	0.9995	0.9953	0.9738	0.9693	0.9781
S2-1	a	0.01	0.01	0.02	0.00	0.00	0.00
	b	2.04	2.06	2.05	2.24	2.32	2.31
	R^2	0.9998	0.9999	0.9999	0.9999	0.9956	0.9991
S3-1	a	0.01	7.38	0.65	0.00	0.00	0.00
	b	2.01	**0.93**	**1.46**	2.10	2.07	2.15
	R^2	0.9985	**0.6484**	**0.9058**	0.9963	0.9813	0.9917
S4-1	a	0.01	0.03	0.04	0.00	0.00	0.00
	b	2.07	1.95	1.99	2.02	2.25	2.17
	R^2	0.9999	0.9660	0.9742	0.9994	0.9912	0.9967
S5-2	a	0.01	0.00	0.00	0.00	0.00	0.00
	b	2.08	3.31	2.82	2.13	2.16	2.18
	R^2	0.9999	0.9716	0.9746	0.9978	0.9979	0.9982
S6-1	a	0.01	0.10	0.06	0.00	0.00	0.00
	b	2.09	**1.69**	**1.88**	2.18	2.22	2.22
	R^2	0.9987	**0.8701**	**0.9472**	0.9989	0.9985	0.9989
S7-1	a	0.00	2.27	0.28	0.00	0.00	0.00
	b	2.25	**1.14**	**1.60**	2.21	2.18	2.24
	R^2	0.9987	**0.6493**	**0.8265**	0.9893	0.9999	0.9974
S8-1	a	0.02	0.01	0.02	0.00	0.00	0.00
	b	1.93	2.21	2.10	2.21	2.26	2.27
	R^2	0.9938	0.9931	0.9869	0.9958	0.9987	0.9979
S9-2	a	0.00	0.02	0.02	0.00	0.01	0.01
	b	2.08	1.90	1.96	2.02	1.92	1.90
	R^2	0.9769	0.9951	0.9993	0.9999	0.9994	0.9999

Fourier transform (FFT) is used to analyse the spectrum of the transient pressure time–history when the HST passes the $FENBRC_{(D=0,\ d=0)}$ and $BILSENB_{(D=0,\ d=2.0H)}$. To facilitate the extension of experimental results to the practical engineering, the Strouhal number St is used to express the frequency [38]:

$$St = \frac{fL}{V} \tag{8}$$

where f is the time-varying frequency of the transient pressure in Hz; L is the characteristic length of the head carriage; and V is the train speed in m/s.

Fig. 23 shows the spectral curve of the aerodynamic pressure on measurement points S1-1, S5-1 and S9-1 when the HST passes through the $FENBRC_{(D=0,\ d=0)}$ at different speeds. Table 6 shows the corresponding St of the dominant frequency. Similar to the head pulse of the $BILSENB_{(D=0,\ d=2.0H)}$, the segment used for FFT is a complete pulse with the highest pressure amplitude extracted from the pressure time–history of the measurement point. As revealed by Fig. 23 and Table 6, the train speed has no significant influence on the dominant frequency of the aerodynamic pressure, and the spectral magnitude generated by the transient pressure on the $FENBRC_{(D=0,\ d=0)}$ is mainly concentrated in the range where St equals 0 to 1.

Under different train speeds, the average St of the dominant frequency of the transient pressure at S5-1 is only 0.06, which is 3–5 times lower than the corresponding value of measurement points S1-1 and S9-1. This phenomenon indicates that the effect of the aerodynamic load caused by the passing HST on measurement point S5-1 lasts longer than measurement points S1-1 and S9-1. In addition, the spectral magnitude of each section increases with the increase in the train speed, and the spectral magnitude of the transient pressure on measurement point S5-1 is the highest, which is approximately 10 and 3 times of measurement points S1-1 and S9-1, respectively.

Fig. 24 shows the spectrum of the head and tail pulses acting on the $BILSENB_{(D=0,\ d=2.0H)}$ and the variation of the St of the dominant frequency with the train speed. The dominant frequency is the frequency when the energy reaches the maximum. The aerodynamic pressure component with the dominant frequency has the most significant aerodynamic impact effect. According to the aforementioned analysis, the HST operation has the most significant impact effect on the bottom area of the noise barrier. Fig. 24(a) shows the spectrum of the transient pressure caused by the HST in Case 9 at three typical measurement points, namely, S1-1, S5-1 and S9-1, and the HST runs at 350 km/h. The aerodynamic impact of the head and tail pulses on the $BILSENB_{(D=0,\ d=2.0H)}$ has a dominant frequency effect, namely, a peak value can be observed in the spectral curve, and the impact energy of the transient pressure is mainly concentrated in the range where St equals 0 to 2. According to previous studies [36], the dominant frequency of the train-induced aerodynamic pressure on the noise barrier is lower than 5 Hz when the train speed is faster than 252 km/h.

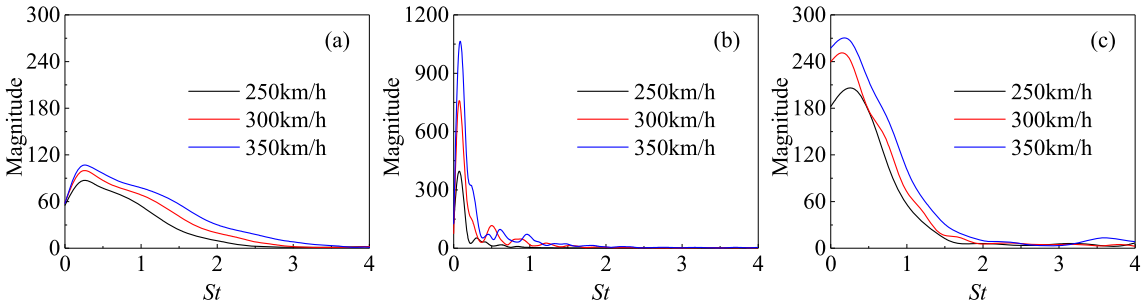

Fig. 23 Train speed effect on the spectral characteristic of $FENBRC_{(D=0,\ d=0)}$: (a) S1-1; (b) S5-1; (c) S9-1.

Table 6 Dominant frequency of train-induced pressure on $FENBRC_{(D=0,\ d=0)}$.

Train speed (km/h)	S1-1	S5-1	S9-1
250	0.207	0.060	0.270
300	0.191	0.060	0.237
350	0.179	0.059	0.255

Correspondingly, the Strouhal number St is lower than 1.78 according to Eq. (8). Therefore, 0 to 2 is deemed to be a correct range for the St of the transient pressure. For S1, S5 and S9 sections, the spectral magnitudes of the head pulse are 77.4 %, 9.2 % and 12.3 % higher than the corresponding values of the tail pulse. Specifically, the aerodynamic impact of the head pulse on the $BILSENB_{(D=0,\ d=2.0H)}$ is more severe than that of the tail pulse.

In Fig. 24(b), St of the dominant frequency of the HST-induced pressure acting on the $BILSENB_{(D=0,\ d=2.0H)}$ ranges approximately from 0.2 to 0.6 when the HST velocity ranges from 250 to 350 km/h. When the train speed changes, the dominant frequencies of head and tail pulses acting on S1 section are significantly different, whereas those on S5 and S9 sections are almost identical, indicating the particularity of the S1 section and further confirming the end effect. The dominant frequency of the head pulse of the S1 section decreased by 25.9 %, that of S5 section only slightly decreased, and that of S9 section increased significantly by 82.0 % with the increase in the train speed to 350 km/h.

In summary, the dominant frequency of the train-induced aerodynamic pressure in the $BILSENB_{(D=0,\ d=2.0H)}$ is higher than that in the $FENBRC_{(D=0,\ d=0)}$. Meanwhile, the spectral magnitude is the highest, and the dominant frequency is the lowest at measurement point S5-1 of the $FENBRC_{(D=0,\ d=0)}$.

Taking measurement point S5-1 as the representative point, Fig. 25(a) shows the spectral magnitude ratio of the $BILSENB_{(D=0,\ d=2.0H)}$ to the $FENBRC_{(D=0,\ d=0)}$, and Fig. 25(b) shows the ratio of St of the dominant frequency. In the figure, M_E and M_F represent the spectral magnitude of the head pulse of the $BILSENB_{(D=0,\ d=2.0H)}$ and $FENBRC_{(D=0,\ d=0)}$, respectively; and St_E and St_F represent

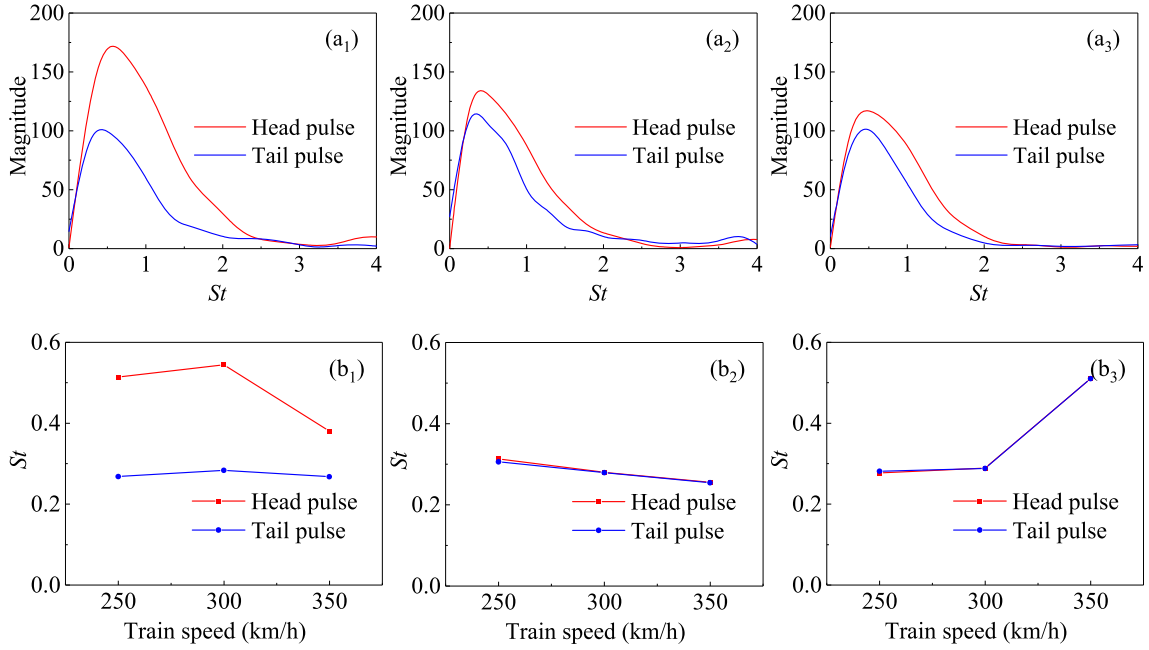

Fig. 24 Spectral characteristic of $BILSENB_{(D=0,\ d=2.0H)}$: (a_1–a_3) spectrum of S1-1, S5-1 and S9-1 in Case; (b_1–b_3) train speed effect on dominant frequency.

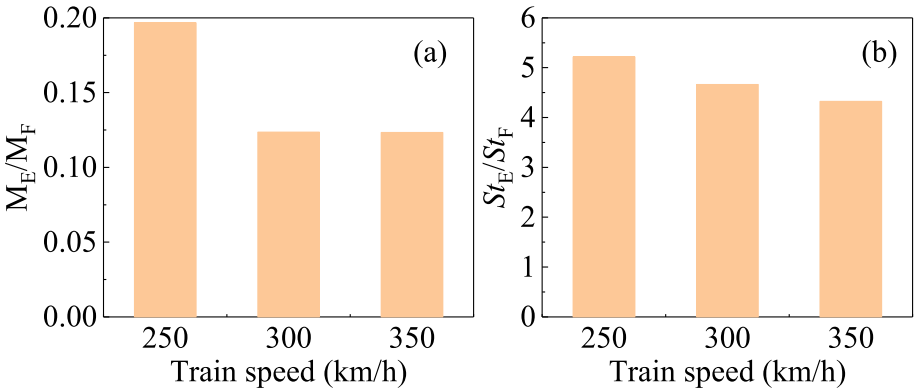

Fig. 25 Spectral comparison of the FENBRC$_{(D=0,\ d=0)}$ and BILSENB$_{(D=0,\ d=2.0H)}$.

the *St* of the dominant frequency of the BILSENB$_{(D=0,\ d=2.0H)}$ and the FENBRC$_{(D=0,\ d=0)}$, respectively. In Fig. 25, the spectral magnitude of the transient pressure generated when the HST passes through the BILSENB$_{(D=0,\ d=2.0H)}$ at 250–350 km/h is approximately 0.12–0.2 times that of the FENBRC$_{(D=0,\ d=0)}$, and the corresponding dominant frequency is 4.3–5.2 times that of the FENBRC$_{(D=0,\ d=0)}$.

4. Discussion

It is worth mentioning that the aforementioned results are obtained based on a CRH380A train. Before the experiment, we have compared the aerodynamic pressure caused by two most frequently used HSTs in China, namely, CRH380A and CRH380B. Fig. 26 compares the aerodynamic pressure caused by the two trains. The adopted train model of CRH380B is presented in Fig. 26(a). As shown in Fig. 26(b), the pressure variation caused by the two types of HSTs is similar and the pressure peaks are also close, indicating the results are not dependent on the type of train. Therefore, we have decided to test all cases using a single type of train, namely, the CRH380A.

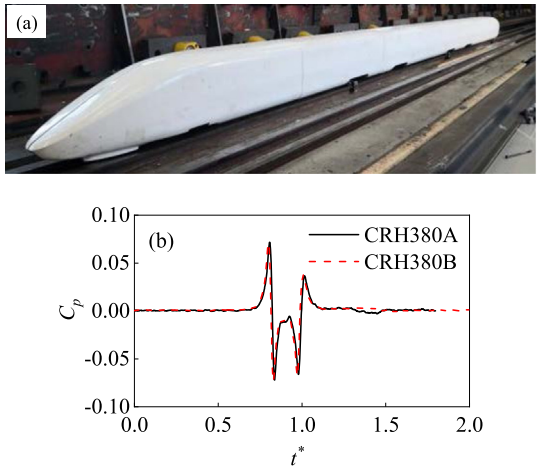

Fig. 26 Comparison of the aerodynamic pressure caused by CRH380A and CRH380B: (a) CRH380B train; (b) pressure.

Based on the results of this research and the literature, we present a comparison between the FENBRC and BILSENB from five aspects, including the aerodynamic performance, life cycle, noise reduction performance, sensitivity to train speeds and economical efficiency. The detailed comparison is summarised in Table 7 and explained as follows:

(1) From the viewpoint of aerodynamic performance and life cycle: The train-induced pressure on the FENBRC is considerably higher than that of BILSENB as revealed by the moving model experiment results. As shown in Fig. 17, the ΔC_p value of the FENBRC is approximately-four times that of the BILSENB. As discussed in Section 3.3, the spectral magnitude of the transient pressure of the BILSENB is only 0.12–0.2 times that of the FENBRC. Therefore, the life cycle of the BILSENB is longer than that of the FENBRC under train-induced aerodynamic loads.

(2) From the viewpoint of noise reduction performance: Li et al. compared the aerodynamic noise reduction performance of semi- and fully-enclosed barriers based on a full-scale experiment [39]. In 2020, Li et al. compared the aerodynamic noise reduction capacity of a nearly-closed barrier and a double-straight barrier, as shown in Fig. 27 [10]. The noise reduction performance of the nearly-closed barrier is higher than that of the double-straight barrier in the far field. As indicated by the two references [10,39], the noise reduction performance of noise barriers increases with the increase in the confinement extent. Therefore, we can conclude that the noise reduction

Table 7 A detailed comparison between FENBRC and BILSENB.

Types of noise barrier	Item				
	Aerodynamic performance	Life cycle	Noise reduction performance	Sensitivity to train speeds	Economical efficiency
FENBRC	Worse	Shorter	Better	Less sensitive	Worse
BILSENB	Better	Longer	Worse	More sensitive	Better

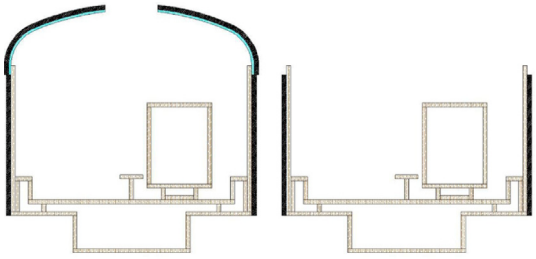

Fig. 27 The nearly-enclosed noise barrier (left) and a double-straight noise barrier (right) [10].

performance of the FENBRC is stronger than that of the BILSENB.

(3) From the viewpoint of sensitive to the train speeds: the transient pressure of the BILSENB is more sensitive to the train speed compared with the FENBRC. As indicated by Section 3.2.2, when applying the power function to fit the positive pressure peak with the train speed, the mean value of the index of the BILSENB is 6.7 % higher than that of the FENBRC on average.

(4) From the viewpoint of economical efficiency: As shown in Figs. 1 and 4, more materials have to be consumed to build a FENBRC because the roof is closed compared with the BILSENB. Therefore, the BILSENB has better economical efficiency compared with the FENBRC.

5. Conclusions

By establishing a 1:16.8 moving model system of the train-noise barrier, we conduct a systematic comparative study on the aerodynamic performance of two types of city-oriented noise barriers when the HST passes by. The train type is CRH380A and the train speed is up to 350 km/h. The main conclusions are as follows:

(1) Inside the FENBRC, the positive pressure peak is generated by the initial compression wave, and the negative pressure peak is caused by the coupling of the expansion wave and the pressure field around the HST. The negative pressure peak is two time that of the positive. The pressure fluctuation on the BILSENB is caused by the impact and adsorption of the airflow when the train passes. The pressure amplitude of the head pulse is 36.67 % higher than that of the tail pulse.

(2) The top opening of the FENBRC has a relief effect on the pressure. The pressure variation range in the FENBRC has a nonlinear relation with opening widths. When the top opening width increases from 0 to 0.5H, the coefficients of pressure amplitude of the entrance and exit sections decrease by 19.5 % and 15.8 %, respectively, and the values decrease by 5.3 % and 8.7 % when the top opening width increases from 1.0H to 1.5H, respectively.

(3) The longitudinal pressure distribution of the FENBRC presents a non-uniform characteristic, namely, small at two ends and large in the middle. The pressure coefficients of the positive peak, negative peak and amplitude of the central section are 13.4 %, 34.4 % and 26.4 % higher than the averages of all points with the same height, respectively. The longitudinal pressure distribution of the BILSENB has an end effect. The coefficients of the positive pressure peak and pressure amplitude of the entrance section are 28.7 % and 14.1 % higher than the average of the other middle section, respectively.

(4) The transient pressure of the BILSENB is more sensitive to the train speed compared with the FENBRC. When applying the power function to fit the positive pressure peak with the train speed, the mean value of the index of the BILSENB is 6.7 % higher than that of the FENBRC on average. For the FENBRC, the positive pressure peak is proportional to the square of the train speed. For the BILSENB, the pressure amplitude at the entrance and exit sections is proportional to the power of 2.73 and 1.90 times of the train speed, respectively.

(5) For the BILSENB, the spectral magnitudes of the head pulse of the entrance, middle and exit sections are 77.4 %, 9.2 % and 12.3 % higher than those of the tail pulse, respectively. For the FENBRC, under different train speeds, the dominant frequency of the transient pressure at the central section is 3–5 times lower than that of the entrance and exit sections under different train speeds, respectively. The dominant frequency of the transient pressure generated when the HST passes through the BILSENB at 250–350 km/h is approximately 4.3–5.2 times that of the FENBRC.

(6) An overall comparison between the two types of noise barriers has been made: The life cycle of the BILSENB is longer than that of the FENBRC under train-induced aerodynamic loads. The noise reduction performance of the FENBRC is stronger than that of the BILSENB. The BILSENB has better economical efficiency compared with the FENBRC.

Notably, this research mainly focuses on the aerodynamic impact of the HST on noise barriers. The noise reduction performance of the noise barriers should be considered in the future. Moreover, numerical simulations will be performed to reveal the flow field mechanism and to further verify the experimental results. The aerodynamic load and response of the HST, affecting the passenger comfort, should also be considered in the future.

CRediT authorship contribution statement

Yikang Liu: Investigation, Writing – original draft. **Weichao Yang:** Conceptualization, Funding acquisition, Writing – review & editing. **E Deng:** Methodology, Data curation, Funding acquisition, Supervision, Writing – review & editing. **Youwu Wang:** Writing – review & editing. **Xuhui He:** Funding acquisition, Writing – review & editing. **Yongming Huang:** Resources, Writing – review & editing. **Zhengwei Chen:** Writing – review & editing.

Declaration of Competing Interest

The authors declare that they have no known competing financial interests or personal relationships that could have appeared to influence the work reported in this paper.

Acknowledgement

This work was funded by the National Natural Science Foundation of China [grant numbers 51978670 and U1934209], Science and Technology Research and Development Program

Project of China railway group limited (Major Special Project, 2021-Special-04-2), the National Outstanding Youth Science Fund Project of National Natural Science Foundation of China [grant number 51925808], the Research Grants Council, University Grants Committee of the Hong Kong Special Administrative Region (SAR), China [grant number R-5020-18], the Innovation and Technology Commission of the Hong Kong SAR Government [grant number K-BBY1] and The Hong Kong Polytechnic University's Postdoc Matching Fund Scheme [grant number 1-W21Q].

References

[1] W.C. Yang, Y.K. Liu, E. Deng, Y.W. Wang, X.H. He, Y.M. Huang, Y.F. Zou, Moving model test on the aerodynamic pressure of bilateral inverted-L-shaped noise barriers caused by high-speed trains, J. Wind Eng. Ind. Aerodyn. 228 (2022) 105083.

[2] W.C. Yang, D.H. Ouyang, E. Deng, Y.W. Wang, Z.W. Chen, X.H. He, Y.M. Huang, Deterioration of aerodynamic performance of a train driving through noise barriers under crosswinds, J. Wind Eng. Ind. Aerodyn. 231 (2022) 105241.

[3] T. Li, D. Qin, W.H. Zhang, J.Y. Zhang, Study on the aerodynamic noise characteristics of high-speed pantographs with different strip spacings, J. Wind Eng. Ind. Aerodyn. 202 (2020) 104191.

[4] T. Li, H. Liang, J. Zhang, J.Y. Zhang, Numerical Study on Aerodynamic Resistance Reduction of High-speed Train Using Vortex Generator, Eng. Appl. Comp. Fluid Mech. (2022) 2153925, https://doi.org/10.1080/19942060.2022.2153925.

[5] T. Li, D. Qin, N. Zhou, J.Y. Zhang, W.H. Zhang, Numerical study on the aerodynamic and acoustic scale effects for high-speed train bodv and pantograph, Appl. Acoust. 2022196 (2022), https://doi.org/10.1016/j.apacoust.2022.108886 108886.

[6] E. Deng, X.Y. Liu, Y.Q. Ni, Y.W. Wang, Z.W. Chen, X.H. He, Buffer scheme for aero-performance deterioration caused by trains passing bilateral vertical noise barriers with crosswinds, Eng. Appl. Comp. Fluid Mech. 17 (1) (2023) 2162585.

[7] X.H. Xiong, A.H. Li, X.F. Liang, J. Zhang, Field study on high-speed train induced fluctuating pressure on a bridge noise barrier, J. Wind Eng. Ind. Aerodyn. 177 (2018) 157–166.

[8] E. Deng, W.C. Yang, M.F. Lei, Z.H. Zhu, P.P. Zhang, Aerodynamic loads and traffic safety of high-speed trains when passing through two windproof facilities under crosswind: a comparative study, Eng. Struct. 188 (2019) 320–339.

[9] E. Deng, W.C. Yang, X.H. He, Z.H. Zhu, L. Zhou, Aerodynamic response of high-speed trains under crosswind in a bridge-tunnel section with or without a wind barrier, J. Wind Eng. Ind. Aerodyn. 210 (1) (2021) 104502.

[10] Q.T. Li, D. Duhamel, Y.Y. Luo, H. Yin, Analysing the acoustic performance of a nearly-enclosed noise barrier using scale model experiments and a 2.5-D BEM approach, Appl. Acoust. 158 (2020) 107079.

[11] Y.K. Liu, W.C. Yang, E. Deng, Y.W. Wang, X.H. He, Y.M. Huang, Y.F. Zou, Aerodynamic characteristics of the train–SENB (semi-enclosed noise barrier) system: A high-speed model experiment and LES study, J. Wind Eng. Ind. Aerodyn. 232 (2023) 105251.

[12] X.S. Huo, T.H. Liu, Z.W. Chen, W.H. Li, J.Q. Niu, H.R. Gao, Aerodynamic characteristics of double-connected train groups composed of different kinds of high-speed trains under crosswinds: A comparison study, Alex. Eng. J. (2022), In press.

[13] W.C. Yang, D.H. Ouyang, E. Deng, X.H. He, Y.F. Zou, Y.M. Huang, Aerodynamic characteristics of two noise barriers (fully enclosed and semi-enclosed) caused by a passing train: A comparative study, J. Wind Eng. Ind. Aerodyn. 226 (2022) 105028.

[14] T. Li, Z.Y. Dai, M.G. Yu, W.H. Zhang, Numerical investigation on the aerodynamic resistances of double-unit trains with different gap lengths, Eng. Appl. Comp. Fluid Mech. 15 (1) (2021) 549–560.

[15] Planning Engineering Consulting + Services China Ltd, Consultation Report of the Noise Barriers in Chinese Railway Passenger Dedicated Line (2007).

[16] N. Yang, X.K. Zheng, J. Zhang, S.S. Law, Q.S. Yang, Experimental and numerical studies on aerodynamic loads on an overhead bridge due to passage of high-speed train, J. Wind Eng. Ind. Aerodyn. 140 (2015) 19–33.

[17] X.Z. Li, M. Wang, J. Xiao, Q.Y. Zou, D.J. Liu, Experimental study on aerodynamic characteristics of high-speed train on a truss bridge: A moving model test, J. Wind Eng. Ind. Aerodyn. 179 (2018) 26–38.

[18] Q. Zhang, C. Su, Y. Wang, Numerical investigation on aerodynamic performance and stability of a sedan under wind–bridge–tunnel road condition, Alex. Eng. J. 59 (5) (2020) 3963–3980.

[19] X.H. Xiong, B. Yang, K.W. Wang, T.H. Liu, Z. He, L. Zhu, Full-scale experiment of transient aerodynamic pressures acting on a bridge noise barrier induced by the passage of high-speed trains operating at 380–420 km/h, J. Wind Eng. Ind. Aerodyn. 204 (2020) 104298.

[20] L. Zhang, M.Z. Yang, J.Q. Niu, X.F. Liang, J. Zhang, Moving model tests on transient pressure and micro-pressure wave distribution induced by train passing through tunnel, J. Wind Eng. Ind. Aerodyn. 191 (2019) 1–21.

[21] M. Zaareer, A.-H. Mourad, Effect of Vehicle Side Mirror Base Position on Aerodynamic Forces and Acoustics, Alex. Eng. J. 61 (2) (2022) 1437–1448.

[22] L. Carassale, M.M. Brunenghi, Dynamic response of trackside structures due to the aerodynamic effects produced by passing trains, J. Wind Eng. Ind. Aerodyn. 123 (2013) 317–324.

[23] T. Gilbert, C. Baker, A. Quinn, Aerodynamic pressures around high-speed trains: the transition from unconfined to enclosed spaces, Proc. Inst. Mech. Eng. Part F-J. Rail Rapid Transit 227 (6) (2013) 609–622.

[24] C. Baker, S. Jordan, T. Gilbert, A. Quinn, M. Sterling, T. Johnson, J. Lane, Transient aerodynamic pressures and forces on trackside and overhead structures due to passing trains. Part 1: Model-scale experiments; Part 2: Standards applications, Proc. Inst. Mech. Eng. Part F-J. Rail Rapid Transit 228 (1) (2014) 37–70.

[25] D. Rocchi, G. Tomasini, P. Schito, C. Somaschini, Wind effects induced by high speed train pass-by in open air, J. Wind Eng. Ind. Aerodyn. 173 (2018) 279–288.

[26] X.F. Liang, X.B. Li, G. Chen, B. Sun, Z. Wang, X.H. Xiong, J. Yin, M.Z. Tang, X.L. Li, S. Krajnovic, On the aerodynamic loads when a high speed train passes under an overhead bridge, J. Wind Eng. Ind. Aerodyn. 202 (2020) 104208.

[27] L.W. Zeng, H.F. Wang, L.Q. Li, W. Guo, F.M. Yi, Experimental study of train-induced pressure acting on the platform screen doors in subway station, Tunn. Undergr. Space Technol. 117 (2021) 104150.

[28] M. Lv, Q. Li, Z. Ning, Z. Ji, Study on the aerodynamic load characteristic of noise reduction barrier on high-speed railway, J. Wind Eng. Ind. Aerodyn. 176 (2018) 254–262.

[29] J. Du, L. Zhang, M.Z. Yang, F. Wu, K. Li, Moving model experiments on transient pressure induced by a high-speed train passing through noise barrier, J. Wind Eng. Ind. Aerodyn. 204 (2020) 104267.

[30] L. Zhang, M.Z. Yang, X.F. Liang, J. Zhang, Oblique tunnel portal effects on train and tunnel aerodynamics based on moving model tests, J. Wind Eng. Ind. Aerodyn. 167 (2017) 128–139.

[31] J. Zhang, J.B. Wang, Q.X. Wang, X.H. Xiong, G.J. Gao, A study of the influence of bogie cut outs' angles on the aerodynamic performance of a high-speed train, J. Wind Eng. Ind. Aerodyn. 175 (2018) 153–168.
[32] T.T. Wang, X.B. Han, L. Zhang, B.S. Qian, Z.K. Sun, H.K. Liu, Effect of non-circular tunnel linings on pressure transients induced by high-speed train passes through a tunnel based on moving model test, J. Wind Eng. Ind. Aerodyn. 214 (2021) 104649.
[33] J.R. Bell, D. Burton, M. Thompson, A. Herbst, J. Sheridan, Wind tunnel analysis of the slipstream and wake of a high-speed train, J. Wind Eng. Ind. Aerodyn. 134 (2014) 122–138.
[34] A. Eltayesh, F. Castellani, M. Burlando, M.B. Hanna, A. Huzayyin, H.M. El-Batsh, M. Becchetti, Experimental and numerical investigation of the effect of blade number on the aerodynamic performance of a small-scale horizontal axis wind turbine, Alex. Eng. J. 60 (4) (2021) 3931–3944.
[35] CEN European Standard, Railway Application-Aerodynamics. Part 4 (2013) 14067–114064.
[36] M. Tokunaga, M. Sogabe, T. Santo, K. Ono, Dynamic response evaluation of tall noise barrier on high speed railway structures, J. Sound Vibr. 366 (2016) 293–308.
[37] J.Q. Niu, D. Zhou, X.F. Liang, Numerical simulation of the effects of obstacle deflectors on the aerodynamic performance of stationary high-speed trains at two yaw angles, Proc. Inst. Mech. Eng. Part F-J. Rail Rapid Transit 232 (3) (2018) 913–927.
[38] Z.J. Guo, T.H. Liu, M. Yu, Z.W. Chen, W.H. Li, X.S. Huo, H. K. Liu, Numerical study for the aerodynamic performance of double unit train under crosswind, J. Wind Eng. Ind. Aerodyn. 191 (2019) 203–214.
[39] X.Z. Li, D.W. Yang, W. Gao, Y.K. Luo, Study on vibration and noise reduction of semi- or fully- enclosed noise barriers of high speed railways, Noise and Vibration, Control 38 (Z1) (2018), in Chinese.